

Research Article

Comparisons of Tensile Fracturing Behaviors of Hydraulic Fully Graded and Wet-Screened Concretes: A Mesoscale Study

Lei Xu ¹, Yongmiao Jin ¹, Shuaizhao Jing ¹, Jie Liu ², Yefei Huang ¹,
and Changqiao Zhou ¹

¹College of Water Conservancy and Hydropower Engineering, Hohai University, Nanjing 210098, China

²Chongqing Surveying and Design Institute of Water Resources, Electric Power and Architecture, Chongqing 400020, China

Correspondence should be addressed to Lei Xu; leixu@hhu.edu.cn

Received 1 February 2018; Accepted 23 April 2018; Published 26 June 2018

Academic Editor: Jun Liu

Copyright © 2018 Lei Xu et al. This is an open access article distributed under the Creative Commons Attribution License, which permits unrestricted use, distribution, and reproduction in any medium, provided the original work is properly cited.

The widely used wet-screening method in the experimental testing of hydraulic fully graded concrete inevitably results in a gap between the real mechanical parameters of hydraulic fully graded concrete specimens and those of the corresponding wet-screened specimens and therefore necessitates the comparative study on their mechanical behaviors. To this end, a two-dimensional mesoscale modeling methodology is developed for simulating the tensile fracturing behaviors of hydraulic fully graded and wet-screened concretes, and extensive Monte Carlo simulations are performed. The individual effects of specimen size variation, variation of gradation and volume fraction of coarse aggregates, and the weaker interfacial transition zones surrounding the large coarse aggregates to be removed by wet-screening are detailed followed by the discussion on the combined effect of these three main factors. All the mean values of the macroscopic mechanical parameters related to tensile fracturing behaviors are found to show significant change in response to wet-screening, and the underlying differentiation mechanism and governing factor(s) are identified. Furthermore, it is shown that the randomness of the investigated parameters can be roughly described by the Gaussian distribution, and the dispersion of each of the investigated parameters of hydraulic fully graded concrete is higher than that of the corresponding wet-screened concrete.

1. Introduction

Fully graded concrete is widely used in the construction of hydraulic structures such as gravity dam and arch dam [1]. Compared to ordinary concrete with the maximum size of aggregate (MSA) no more than 40 mm, hydraulic fully graded concrete (hereinafter referred to as HFGC) employs larger coarse aggregates. Typically, the MSA reaches to 80 mm in the case of hydraulic three-graded concrete, while for the four-graded case, the MSA is even larger and increases up to 150 mm (or 120 mm). Moreover, HFGC is also featured by high volume fraction of aggregates composed of fine aggregates and coarse aggregates with the cutoff size between them taken to be 5 mm, low cement content, large admixture dosage, and high water-to-cement ratio [2]. As a result, the mechanical behaviors of HFGC are different from those of the extensively studied ordinary concrete [3]. Thus, to obtain the fundamental mechanical parameters especially the parameters related to fracturing behaviors,

which are needed by the failure analysis of hydraulic mass concrete structures, a detailed investigation on the mechanical behaviors of HFGC is required [4, 5].

With regard to identifying the mechanical parameters of concrete, the larger aggregate size implies that a larger size of concrete specimens, typically at least three times of MSA, is needed to fulfill the requirement of statistical representations [6]. According to the Chinese code SL 352-2006 (test code for hydraulic concrete), the length of specimens L with cube shape for hydraulic three-graded concrete should be set to 300 mm, while for the four-graded case, L is further increased to 450 mm. Compared to the standard specimen with L equal to 150 mm prepared for ordinary concrete, the larger specimen for HFGC causes particular challenges when conducting experimental testing in the usual concrete laboratory, including large size of the testing machine, inconvenience of testing operation, and high testing expense, which further hampers to a large extent the direct experimental testing on HFGC specimens [7].

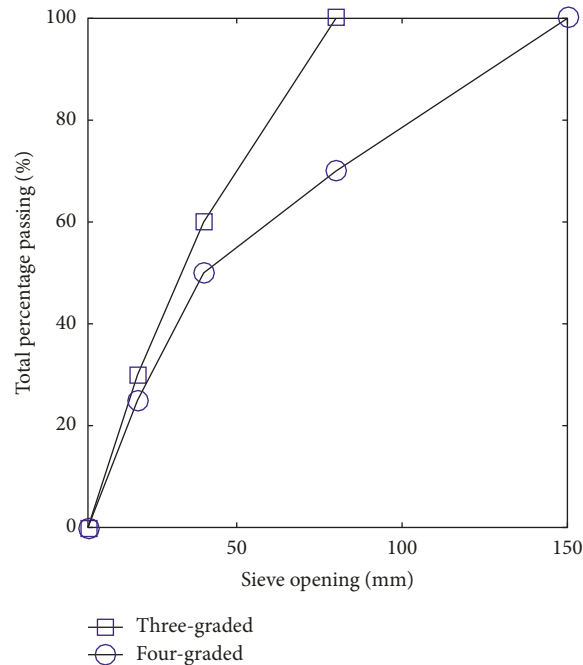


FIGURE 1: Typical coarse aggregate grading curves for hydraulic fully graded concrete.

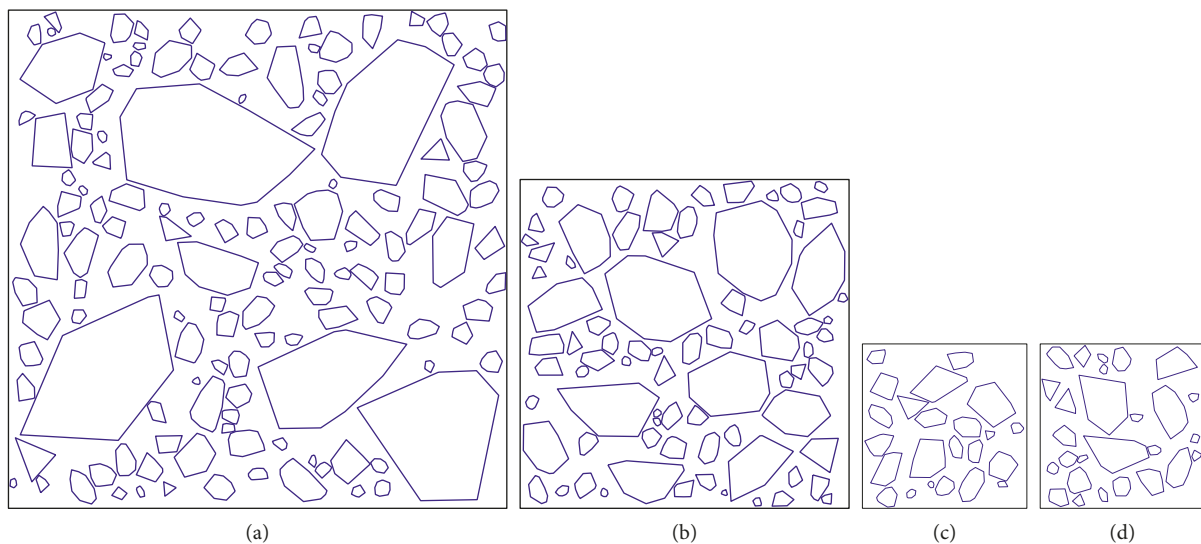


FIGURE 2: Hydraulic fully graded and wet-screened concrete specimens. (a) Four-graded specimen ($A_F = 50\%$, $L = 450$ mm). (b) Three-graded specimen ($A_F = 50\%$, $L = 300$ mm). (c) Wet-screened specimen corresponding to the four-graded specimen ($A_F = 33.3\%$, $L = 150$ mm). (d) Wet-screened specimen corresponding to the three-graded specimen ($A_F = 37.5\%$, $L = 150$ mm).

As an alternative to carrying out mechanical experiments on large specimens, the well-known wet-screening method is commonly employed in practice [8]. Following this method, experimental testing is performed on standard specimens, which are cast using the wet-screened concrete obtained by removing the coarse aggregates with the size larger than 40 mm from the original fully graded concrete through sieving, enabling the testing under usual laboratory conditions. Although the wet-screening method can avoid the direct testing on large specimens, a gap inevitably exists [9] between the real mechanical parameters of HFGC specimens and those of the corresponding wet-screened specimens;

that is, the standard specimens cast using the wet-screened concrete. Therefore, an extrapolation procedure should be executed with the aim of acquiring the accurate characterization of the mechanical properties of HFGC [10], which necessitates a detailed comparative study on the mechanical parameters of hydraulic fully graded and wet-screened concretes [11].

In spite of the awareness of the differences between the mechanical parameters of HFGC and those of the corresponding wet-screened concrete, related experimental comparisons are still sparse due to the practical difficulties of performing extensive large-scale tests. Pioneered by Blanks

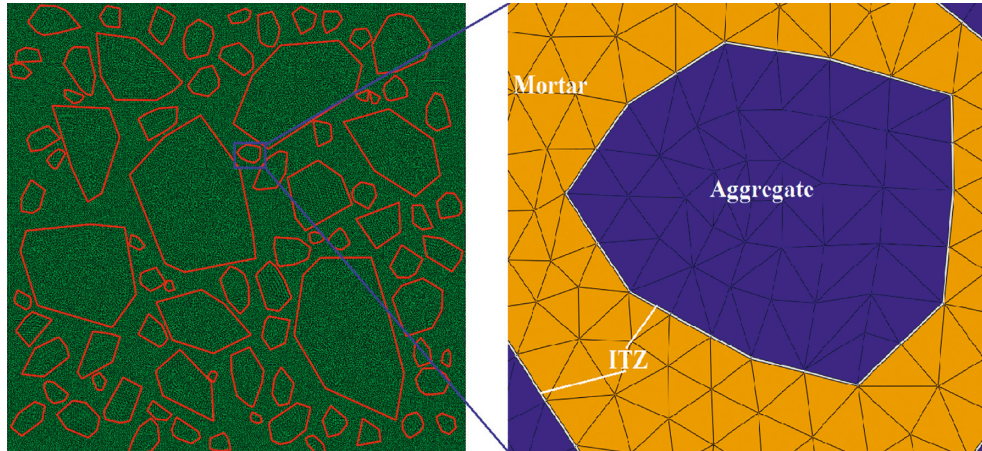


FIGURE 3: FE mesh discretization.

and McNamara [12], limited comparative experimental results can be found in [13–17], and the most recent representative investigations were carried out by Deng et al. [18] who presented the behaviors of dam and sieved concretes in uniaxial tension and compression together with the effects of curing age, by Serra et al. [19] who studied the influence of the wet-screening of the dam concrete on the development of the modulus of elasticity based on a specific experimental program using in situ creep cells, and by Shi et al. [20] who performed experimental study on uniaxial compression properties of large aggregates and wet-screened concrete at different strain rates. On the whole, although it has been well accepted that the differences mentioned above are mainly attributed to specimen size variation, variation of gradation and volume fraction of coarse aggregate, and the weaker interfacial transition zones (ITZs) surrounding large coarse aggregate particles in HFGC [21], the individual effect of these three factors, which can provide fundamental knowledge of the underlying differentiation mechanism, has been rarely studied in the past experimental research works. Furthermore, being aware of the fact that the mechanical parameters of concrete are intrinsically random, it is necessary to compare the mechanical parameters of HFGC and the corresponding wet-screened concrete in the statistical sense, which, to the best of our knowledge, has not been conducted.

On the contrary, since the mechanical behaviors of concrete on the structural scale (macroscale) are greatly controlled by its components and their interactions taking place on a finer scale (mesoscale) [22, 23], several mesoscale models have been developed to provide tools for a better understanding of the extremely complicated mechanical behaviors of concrete, especially fracturing [24]. Roughly, there are two types of mesoscale models, namely, the continuum model [25–28] and the lattice model [29–31]. In the continuum model, concrete is usually characterized by a continuum composite material with each component discretized by finite elements, while for the lattice model, a discrete system composed of lattice elements is used to represent concrete. On the whole, both of them are capable of realizing reasonable simulations of microcracking,

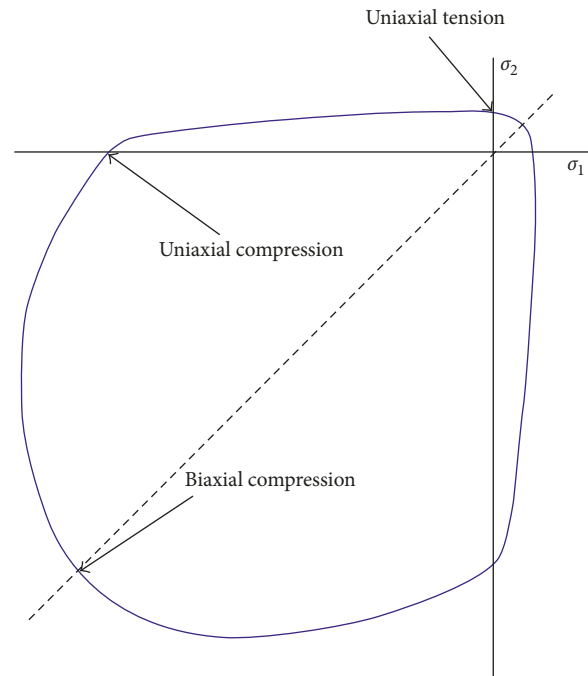


FIGURE 4: Yield surface in plane stress.

coalescence of multiple distributed cracks into localized cracks, and fracture propagation, provided each component in concrete is modeled with use of a well-suited mechanical model. In contrast to the continuum model, the lattice model is considered computationally less demanding as concrete mesostructure is roughly represented by a discrete system with relatively less degrees of freedom and meanwhile can still possess the ability to capture the most important aspects of concrete fracturing. However, it is hard to investigate the interactions of concrete components in a real sense as the actual concrete mesostructure is not fully taken into account. Consequently, mesoscale numerical simulation using the continuum model can be considered as a promising complement to experimental testing in the comparative study on the mechanical parameters of HFGC and wet-screened concrete.

TABLE 1: Mechanical properties of concrete components.

Material	E_0 (GPa)	Poisson's ratio (—)	σ_{t0} (MPa)	ϵ (—)	ψ (°)	α (—)	γ (—)
Aggregate	50	0.2	—	—	—	—	—
Mortar	20	0.2	1.94	0.1	35	0.12	2.0
ITZ	15	0.2	1.46	0.1	35	0.12	2.0

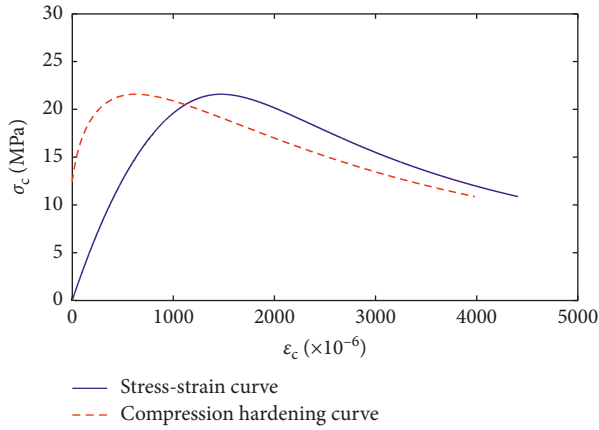


FIGURE 5: Total stress-strain relation under uniaxial compression and compression hardening curve of mortar.

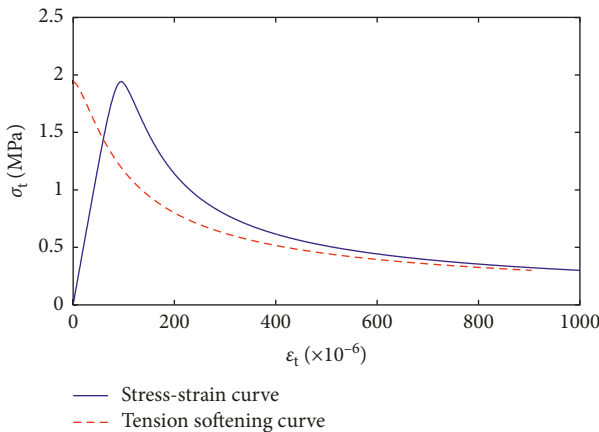


FIGURE 6: Total stress-strain relation under uniaxial tension and tension softening curve of mortar.

Considering this, a two-dimensional (2D) finite element (FE) mesoscale modeling framework for hydraulic fully graded and wet-screened concretes is proposed in this study, in which concrete is considered as a three-phase composite composed of coarse aggregate, mortar, and ITZ, and comprehensive comparisons of tensile fracturing behaviors of HFGC and the wet-screened concrete are performed based on extensive Monte Carlo simulations (MCS).

2. Mesostructure Generation of HFGC and Wet-Screened Concrete

To explicitly model the components and their interactions of both HFGC and the wet-screened concrete on the mesoscale, the internal material structure of concrete should be generated. In this regard, concrete is considered to be

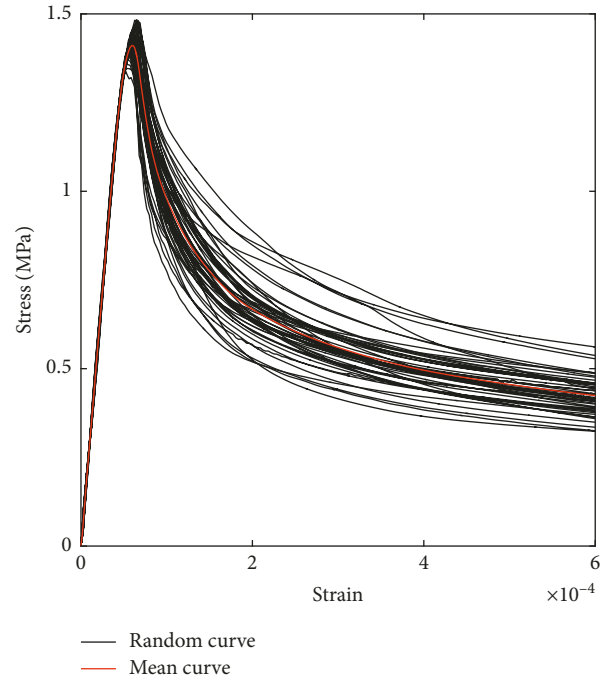


FIGURE 7: Macroscopic stress-strain curves and their mean curve of Type I.

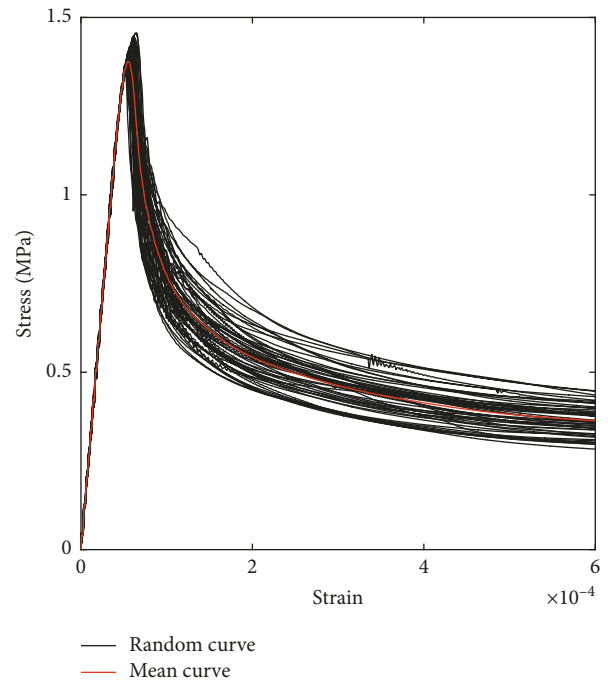


FIGURE 8: Macroscopic stress-strain curves and their mean curve of Type II.

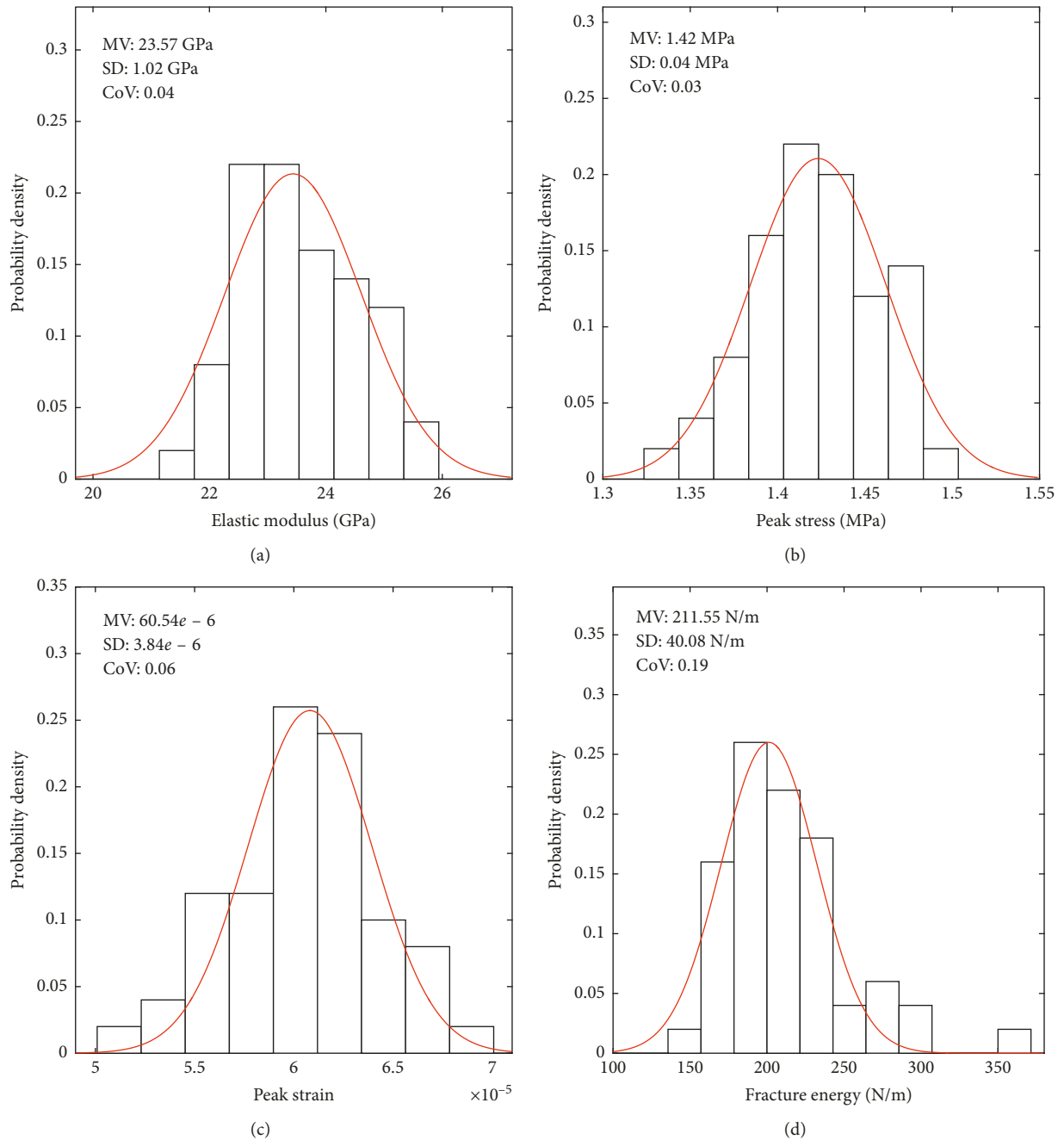


FIGURE 9: Probability density of macroscopic mechanical parameters related to tensile fracturing behaviors of Type I. (a) Tensile elastic modulus. (b) Peak stress. (c) Peak strain. (d) Fracture energy.

a composite consisting of the homogeneous mortar matrix representing cement paste and fine aggregates, randomly distributed coarse aggregates, and ITZs surrounding coarse aggregates. For a specimen, the key issue in generating its internal material structure is to determine the configuration of coarse aggregates, given the size and spatial distributions, volume fraction, and geometric characteristics of the coarse aggregate.

Unlike ordinary concrete usually adopting the well-known Fuller’s curve, the size distribution of coarse aggregates of HFGC is commonly described by three or four

grading segments with fixed maximum and minimum aggregate sizes for each segment. With respect to hydraulic three-graded concrete, coarse aggregates are divided into three groups: the small coarse aggregate with size ranging from 5 to 20 mm, the medium coarse aggregate with size ranging from 20 to 40 mm, and the large coarse aggregate with size ranging from 40 to 80 mm, while regarding the four-graded case, another group of coarse aggregate with even larger size ranging from 80 to 150 mm (or 120 mm), namely, the extra-large coarse aggregate, is used besides the above three groups. In addition, it is usually assumed that

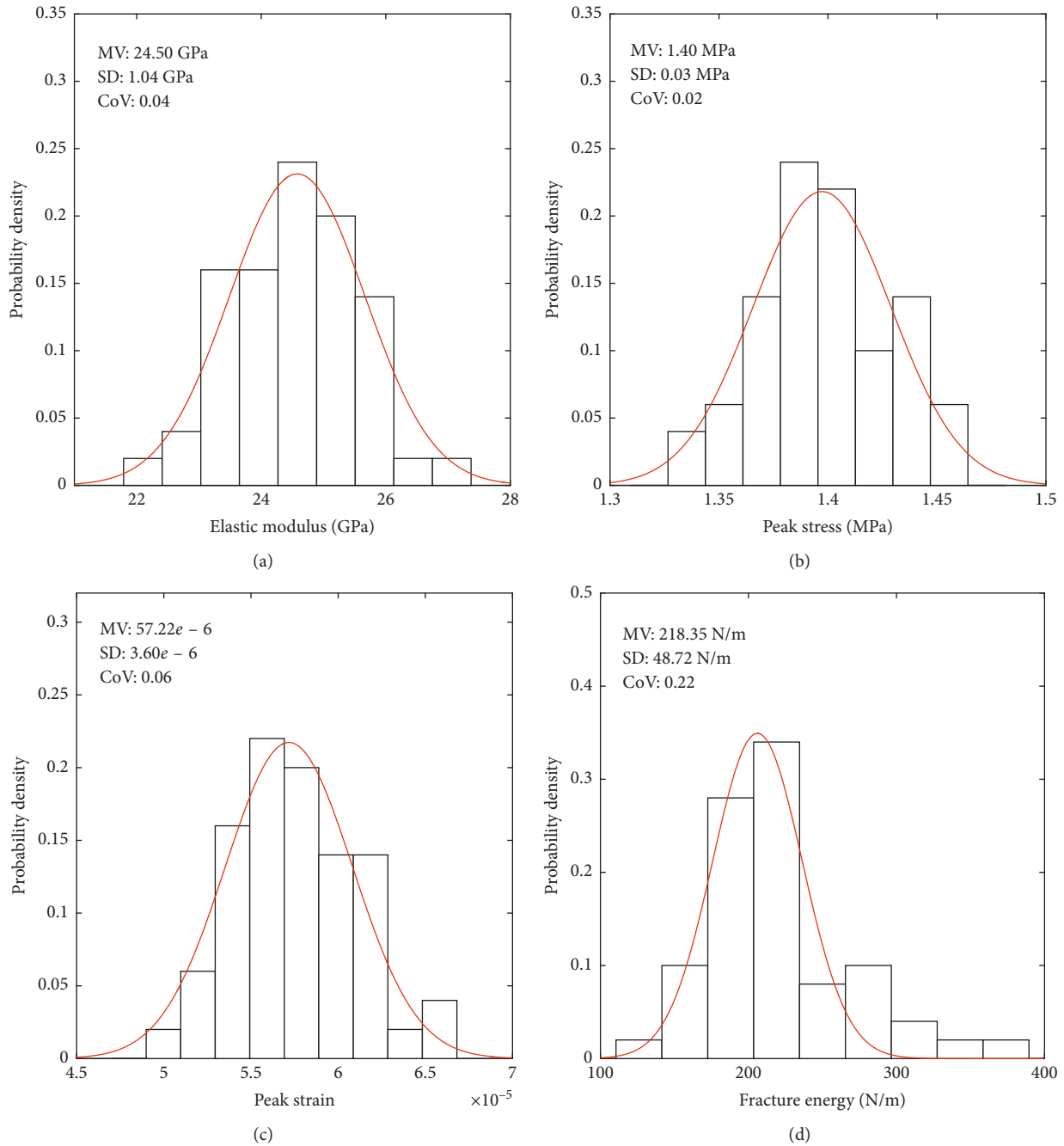


FIGURE 10: Probability density of macroscopic mechanical parameters related to tensile fracturing behaviors of Type II. (a) Tensile elastic modulus. (b) Peak stress. (c) Peak strain. (d) Fracture energy.

the size of the coarse aggregate in a certain segment follows the uniform distribution as the size distribution of the coarse aggregate for each segment is commonly not precisely controlled during the production of HFGC. Hence, on the basis of the given coarse aggregate weight of each grading segment, the size distribution of coarse aggregate can be determined with ease. Figure 1 depicts two typical coarse aggregate grading curves corresponding to hydraulic three- and four-graded concretes, respectively. While for the wet-screened concrete, the coarse aggregate gradation can be calculated in a straightforward way, by removing grading

segment(s) with size larger than 40 mm from the coarse aggregate gradation of HFGC.

Concerning the spatial distribution of coarse aggregates, it is well accepted that coarse aggregates can be considered to be randomly distributed in a certain specimen. Consequently, the location of an individual coarse aggregate needed to be placed in the specimen, which can be represented by the coordinates of its geometric center, is assumed to be uniformly distributed throughout the specimen in this study.

For a given concrete mix design, the volume fraction of coarse aggregate in the three-dimensional (3D) sense can be

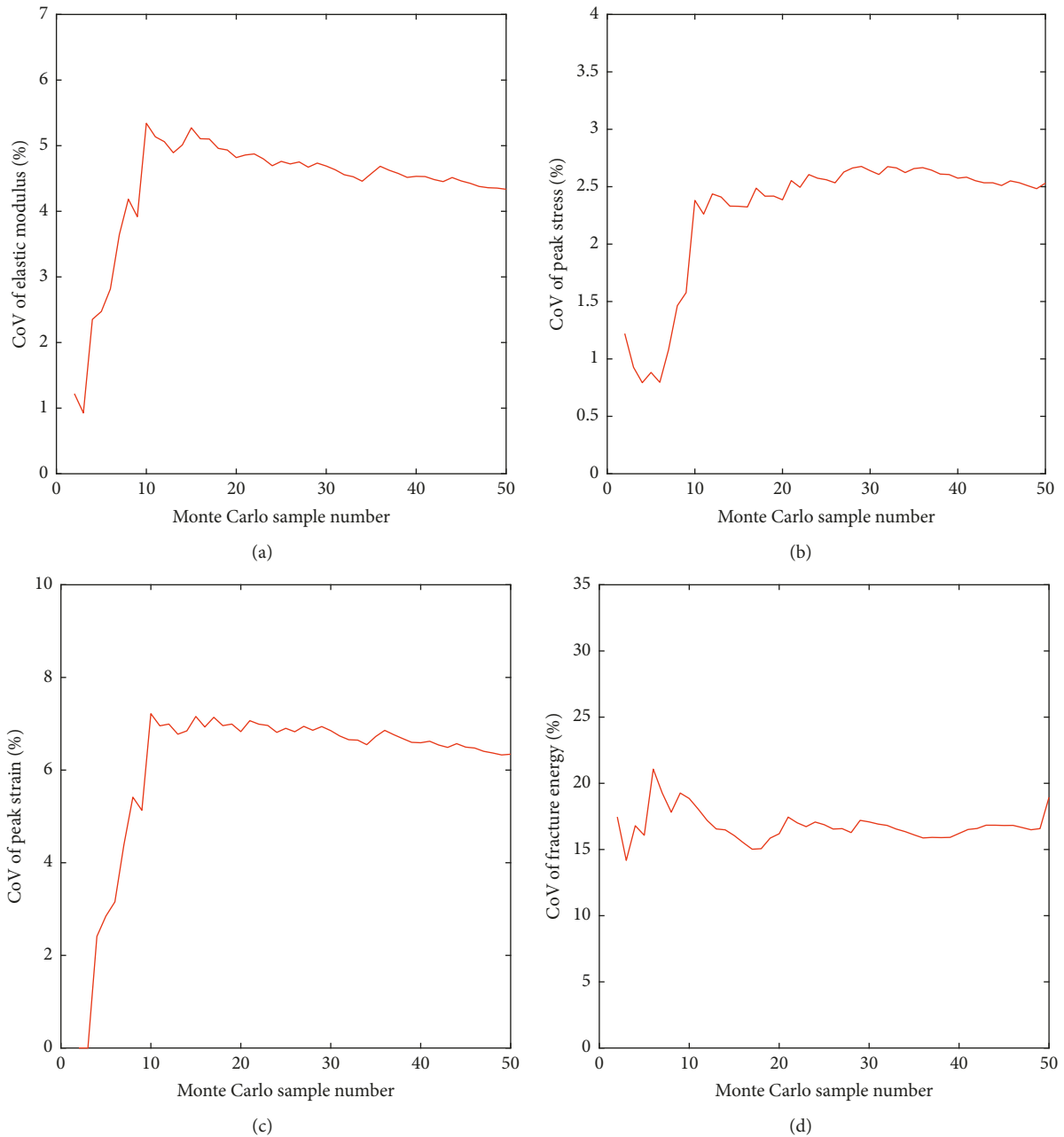


FIGURE 11: Influence of the sample number on CoVs of macroscopic mechanical parameters of Type I. (a) Tensile elastic modulus. (b) Peak stress. (c) Peak strain. (d) Fracture energy.

directly calculated through dividing the total weight of coarse aggregate used in a unit volume of concrete by its unit weight. However, for the simplified two-dimensional case, a conversion of the volume fraction of coarse aggregate from 3D to 2D should be conducted. To this end, the well-known Walraven's conversion equation used by several researchers is employed in the present work [32].

The existing studies indicate that the shape of coarse aggregate affects the mechanical behaviors of concrete, especially the mesoscale fracture mechanism [24]. Regarding HFGC, there are mainly two types of coarse aggregates: the gravel stone and the crushed stone. In the 2D case, an ellipse

can be utilized to represent the gravel stone, while the crushed stone can be simplified to a polygon. Due to the fact that the crushed stone is more commonly used in practice compared to the gravel one, the shape of the coarse aggregate in this study is modeled by the polygon.

After determining the gradation and volume fraction of the coarse aggregate along with the shape and size of the concrete specimen, the required concrete mesostructure can be randomly generated by employing the widely used parameterized modeling approach based on the take-and-place method [33]. In this study, the versatile mesostructure generator for concrete (MGC), developed using MATLAB, is

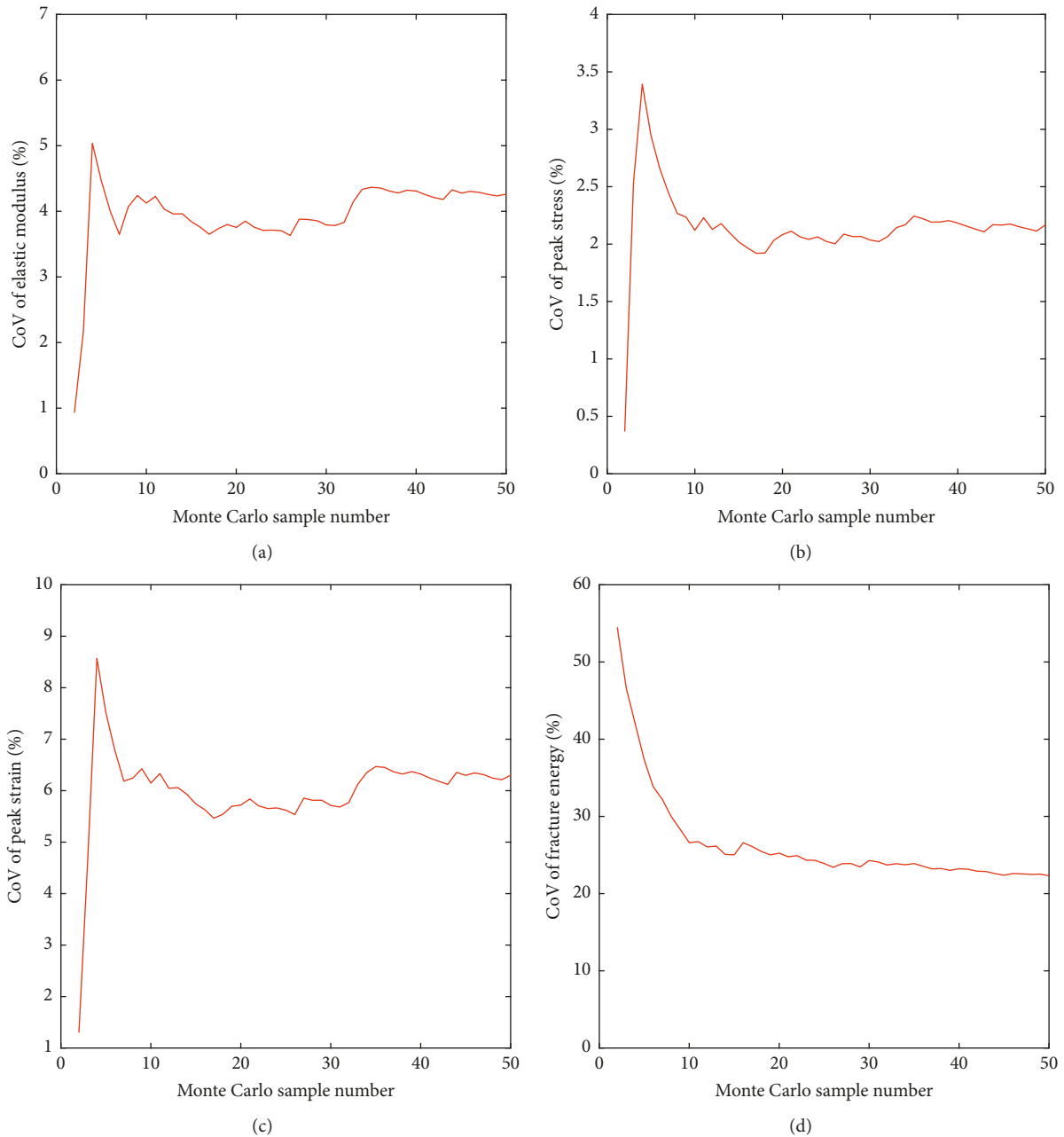


FIGURE 12: Influence of sample number on CoVs of macroscopic mechanical parameters of Type II. (a) Tensile elastic modulus. (b) Peak stress. (c) Peak strain. (d) Fracture energy.

used to generate the following required HFGC specimens and the wet-screened concrete specimens, and the detailed procedure and implementation of MGC can be referred to our previous work [34]. Figure 2(a) sketches an example of a hydraulic four-graded concrete specimen with the coarse aggregate volume fraction $A_F = 50\%$ and the proportions of the small, medium, large, and extra-large coarse aggregates set to 0.25, 0.25, 0.2, and 0.3, respectively, while an example of a hydraulic three-graded concrete specimen with the same coarse aggregate volume fraction and the proportions of the small, medium, and large coarse aggregates set to 0.3, 0.3, and 0.4, respectively, is illustrated in Figure 2(b). The wet-screened

concrete specimens corresponding to the above two examples are shown in Figures 2(c) and 2(d), respectively.

3. Finite Element Modeling Methodology and Monte Carlo Simulations

Provided the mesostructure of a concrete specimen, the corresponding computational model is needed for performing the following mesoscale study. A 2D mesoscale FE modeling methodology for tensile fracturing simulations is developed in this section. Moreover, the Monte Carlo method is employed to take into account the randomness of

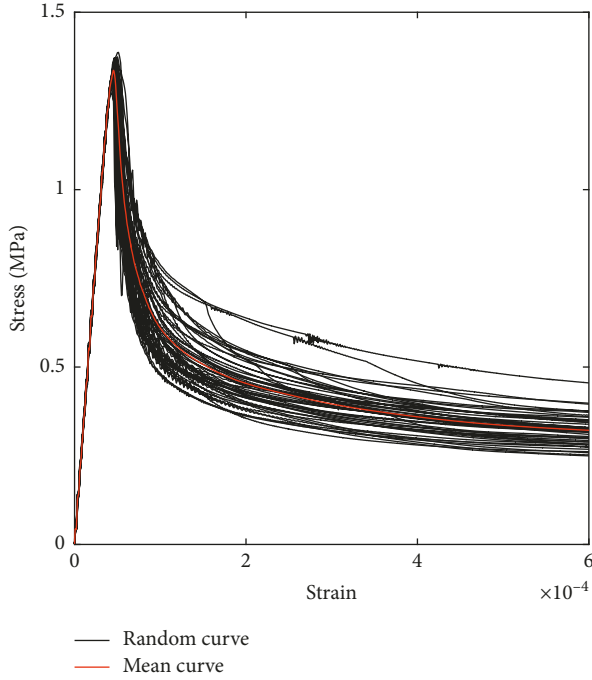


FIGURE 13: Macroscopic stress-strain curves and their mean curve of Type III.

concrete mesostructure and to obtain statistical characteristics of the macroscopic mechanical parameters related to tensile fracturing behaviors, serving as the basis of the subsequent comparative study.

3.1. Mesh Discretization. In order to realize the precise mesh discretization of the generated HFGC and wet-screened concrete specimens, a two-step meshing approach is proposed, by which the accurate representation of concrete mesostructure in the FE model can be achieved. Firstly, an original FE mesh including coarse aggregates and mortar, rigidly obeying the given arrangement of coarse aggregates, is generated by exploiting the powerful preprocessing modules provided by the commercial finite element software ABAQUS. Then, the thin-layer four-node elements with a uniform thickness approximately set to $100 \mu\text{m}$ according to the experimental observation [35], which are used to model ITZs, are automatically inserted between coarse aggregate elements and their surrounding mortar elements. Following this strategy, a mesh generator is developed using MATLAB and Python, with the detailed procedure and implementation described in the previous study [34]. Moreover, in order to ensure the accurate representation of the geometric characteristics of coarse aggregates and meanwhile to generate a computationally less demanding FE model, the distance between two neighbouring seeds along the edges of coarse aggregates and the boundary of the specimen, which controls the average element size (or mesh density) to a great extent, is set to 0.4 times of the minimum size of the coarse aggregate. An example of the final FE mesh discretization with ITZ elements highlighted and the zooming image of a part of the FE mesh are depicted in Figure 3.

3.2. Constitutive Modeling. Concerning concrete fracturing, it is well recognized that mesoscale cracking under loading first appears in ITZs owing to their weaker properties. Afterwards, the existing cracks propagate into mortar and additional cracks may initiate within mortar during the process of further loading, while coarse aggregates commonly behave elastically. Thus, the mechanical behavior of coarse aggregates is simulated herein by the isotropic linear elastic model, whereas a continuum damaged plasticity (CDP) model implemented in ABAQUS [36] is used to describe the mechanical behaviors of both mortar and ITZ, which is briefly summarized below.

In the CDP model, two independent hardening variables, that is, equivalent compressive and tensile plastic strains ($\bar{\varepsilon}_c^p$ and $\bar{\varepsilon}_t^p$), are employed in order to consider compressive crushing and tensile cracking, respectively. Then, two independent damage variables d_c ($\bar{\varepsilon}_c^p$) and d_t ($\bar{\varepsilon}_t^p$) are introduced to characterize the compressive and tensile damage states. In addition, to represent the overall damage in an isotropic manner, a scale variable d is defined as

$$d = 1 - (1 - s_t d_c)(1 - s_c d_t), \quad (1)$$

where s_t and s_c are the functions of the stress state which are used to represent stiffness recovery effects associated with stress reversals [37].

Thus, the damaged elastic modulus E related to different failure mechanisms under tension and compression can be calculated by

$$E = (1 - d)E_0, \quad (2)$$

where E_0 represents the initial elastic modulus.

Based on the concept of damage mechanics, the effective stress $\bar{\sigma}$ can be obtained as

$$\bar{\sigma} = \frac{\sigma}{1 - d}, \quad (3)$$

where σ is the Cauchy stress.

The yield function of the CDP model is given in the effective stress space as

$$F(\bar{\sigma}, \bar{\varepsilon}^p) = \frac{1}{1 - \alpha} (\bar{q} - 3\alpha\bar{p} + \beta(\bar{\varepsilon}^p) \langle \bar{\sigma}_{\max} \rangle - \gamma \langle -\bar{\sigma}_{\max} \rangle) - \bar{\sigma}_c(\bar{\varepsilon}_c^p), \quad (4)$$

where $\bar{\varepsilon}^p = [\bar{\varepsilon}_t^p \cdot \bar{\varepsilon}_c^p]^T$; \bar{p} and \bar{q} are the effective hydrostatic pressure and the effective Mises equivalent deviatoric stress, respectively; $\bar{\sigma}_{\max}$ is the algebraically maximum eigenvalue of $\bar{\sigma}$; the brackets $\langle \rangle$ are used in Macaulay sense; $\bar{\sigma}_c(\bar{\varepsilon}_c^p)$ is the uniaxial compressive effective strength; α and γ are the dimensionless material constants, which can be determined by comparing the initial equibiaxial and uniaxial compressive yield stress and by comparing the yield conditions along the tensile and compressive meridians, respectively; and $\beta(\bar{\varepsilon}^p)$ can be calculated by

$$\beta(\bar{\varepsilon}^p) = \frac{\bar{\sigma}_c(\bar{\varepsilon}_c^p)}{\bar{\sigma}_t(\bar{\varepsilon}_t^p)} (1 - \alpha) - (1 + \alpha), \quad (5)$$

where $\bar{\sigma}_t(\bar{\varepsilon}_t^p)$ is the uniaxial tensile effective strength. Figure 4 illustrates the yield surface in the case of plane stress.

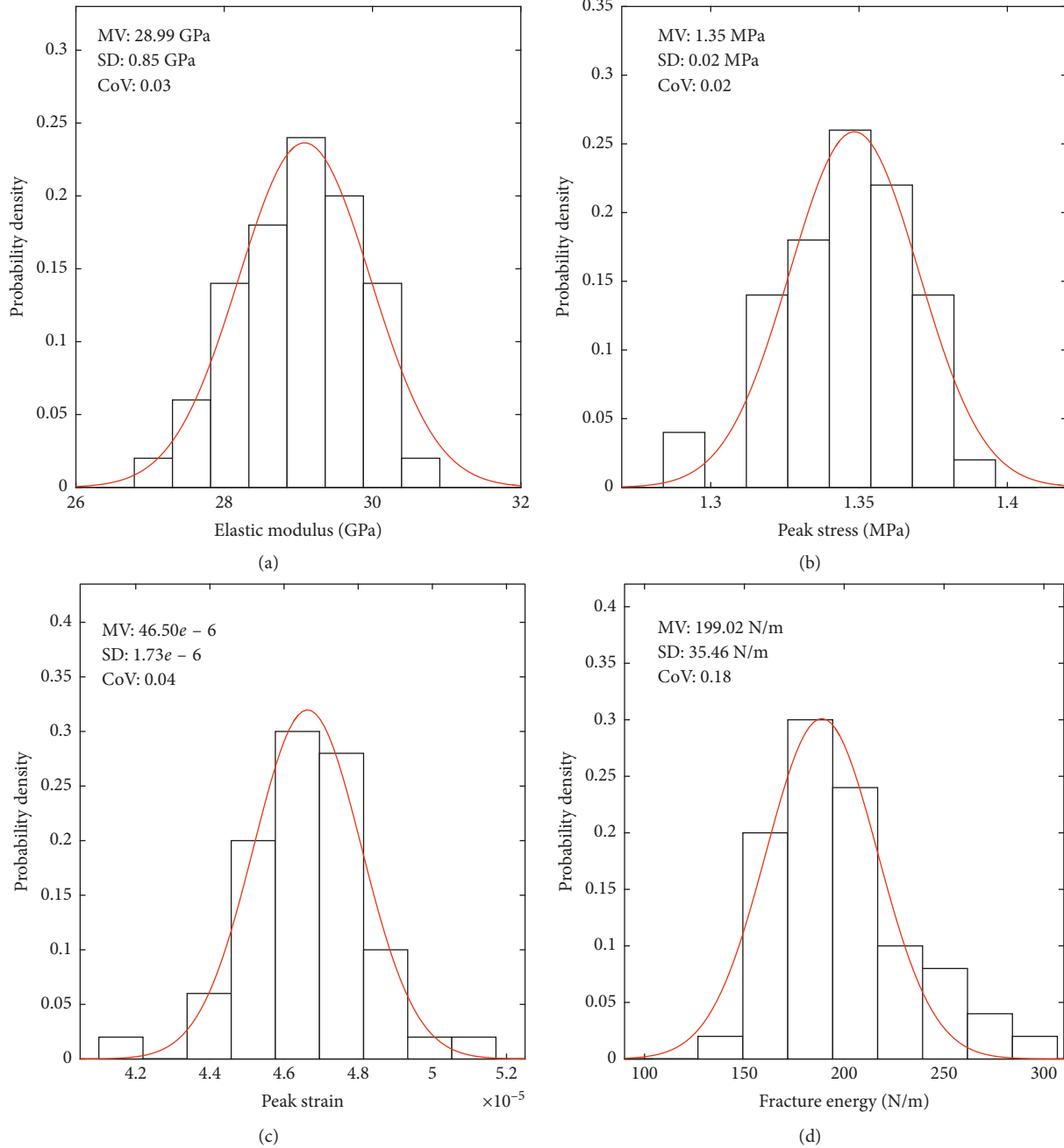


FIGURE 14: Probability density of macroscopic mechanical parameters related to tensile fracturing behaviors of Type III. (a) Tensile elastic modulus. (b) Peak stress. (c) Peak strain. (d) Fracture energy.

In order to describe the dilatancy reasonably, the non-associated flow rule is adopted in the CDP model, and the flow potential is formulated as

$$G(\bar{\sigma}) = \sqrt{(\epsilon \sigma_{t0} \tan \psi)^2 + \bar{q}^2} - \bar{p} \tan(\psi), \quad (6)$$

where ϵ is the parameter defining the rate at which the function approaches the asymptote; σ_{t0} is the uniaxial tensile stress at failure; ψ is the dilation angle measured in the $\bar{p}-\bar{q}$ plane at high confining pressure.

As stated earlier, the material softening under tension is defined by the relationship between the uniaxial tensile

effective strength and equivalent tensile plastic strain (5), which means mesh sensitivity will be encountered when applying the CDP model in FE simulations. Therefore, a stress-displacement relation is used in this study to define the tensile softening behavior for alleviating the influence of mesh sensitivity on the simulation results.

3.3. Numerical Solution Algorithm. Owing to the highly nonlinear and softening behavior of concrete in the process of tensile fracturing, the ABAQUS/Explicit solver is employed in the present work in order to capture the entire fracturing process.

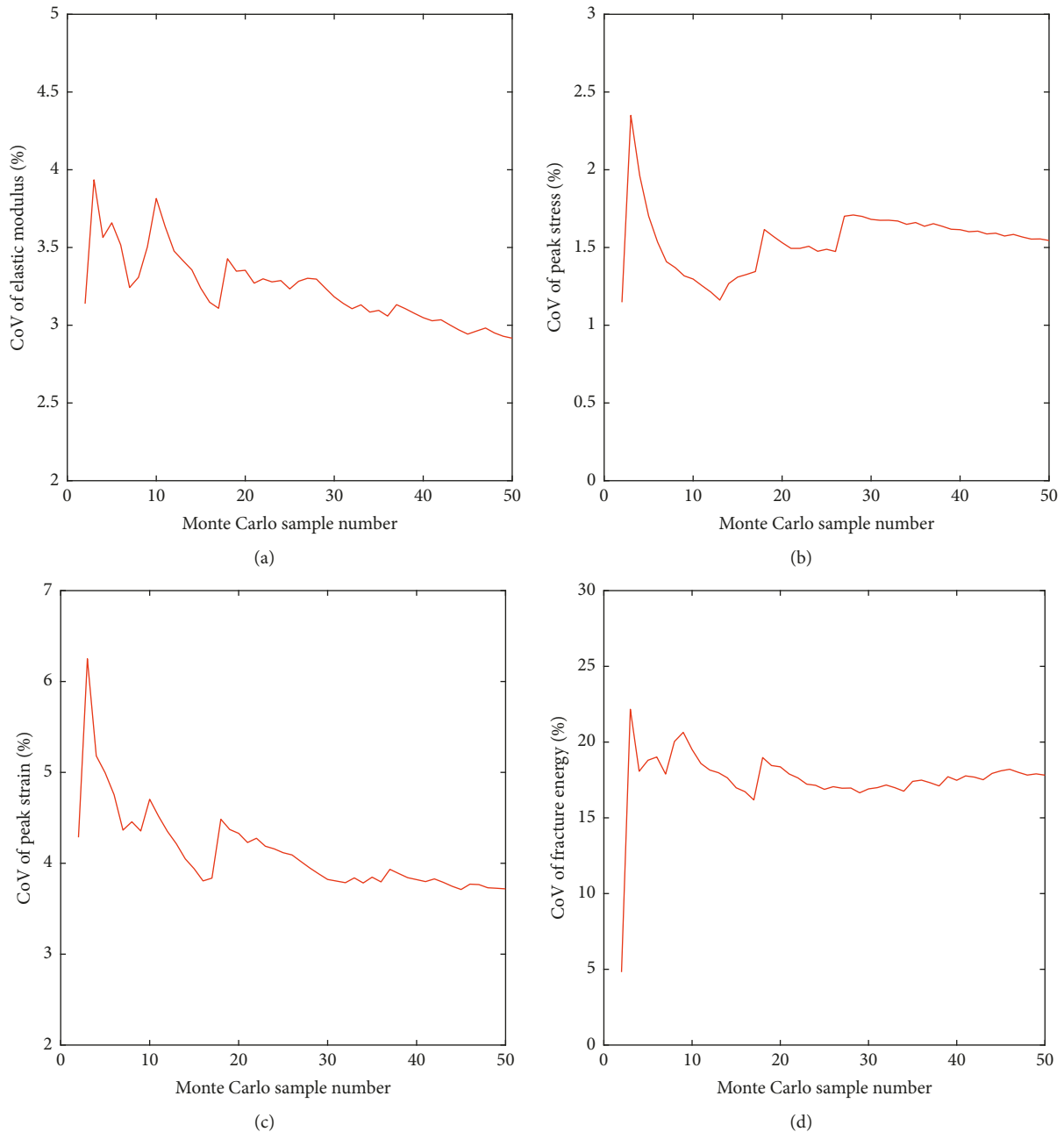


FIGURE 15: Influence of the sample number on CoV of macroscopic mechanical parameters of Type III. (a) Tensile elastic modulus. (b) Peak stress. (c) Peak strain. (d) Fracture energy.

Regarding the explicit FE modeling, the dynamic effect inevitably exists, and therefore, its influence on the solution of a quasistatic problem should be small enough to be neglected. In order to minimize the dynamic effect, the loading duration should be large enough, while on the other hand, the computational effort increases proportionally with the increase of loading duration. Hence, a balance has to be made between the computational efficiency and simulation accuracy, which can be achieved through comparing the results under different loading durations (or loading rates).

3.4. Monte Carlo Simulations and Statistical Analysis. Due to the random arrangement of coarse aggregates, the mechanical behaviors of concrete obtained from both experimental testing and numerical modeling vary with specimens having the same size, especially in the nonlinear regime, which consequently necessitates the analysis of concrete mechanical behaviors in a statistical sense in order to get more conclusive and accurate results. Hence, the Monte Carlo simulations are conducted in this study aiming at obtaining the statistical characteristics of the mechanical parameters related to tensile fracturing behaviors of both HFGC and wet-screened concrete.

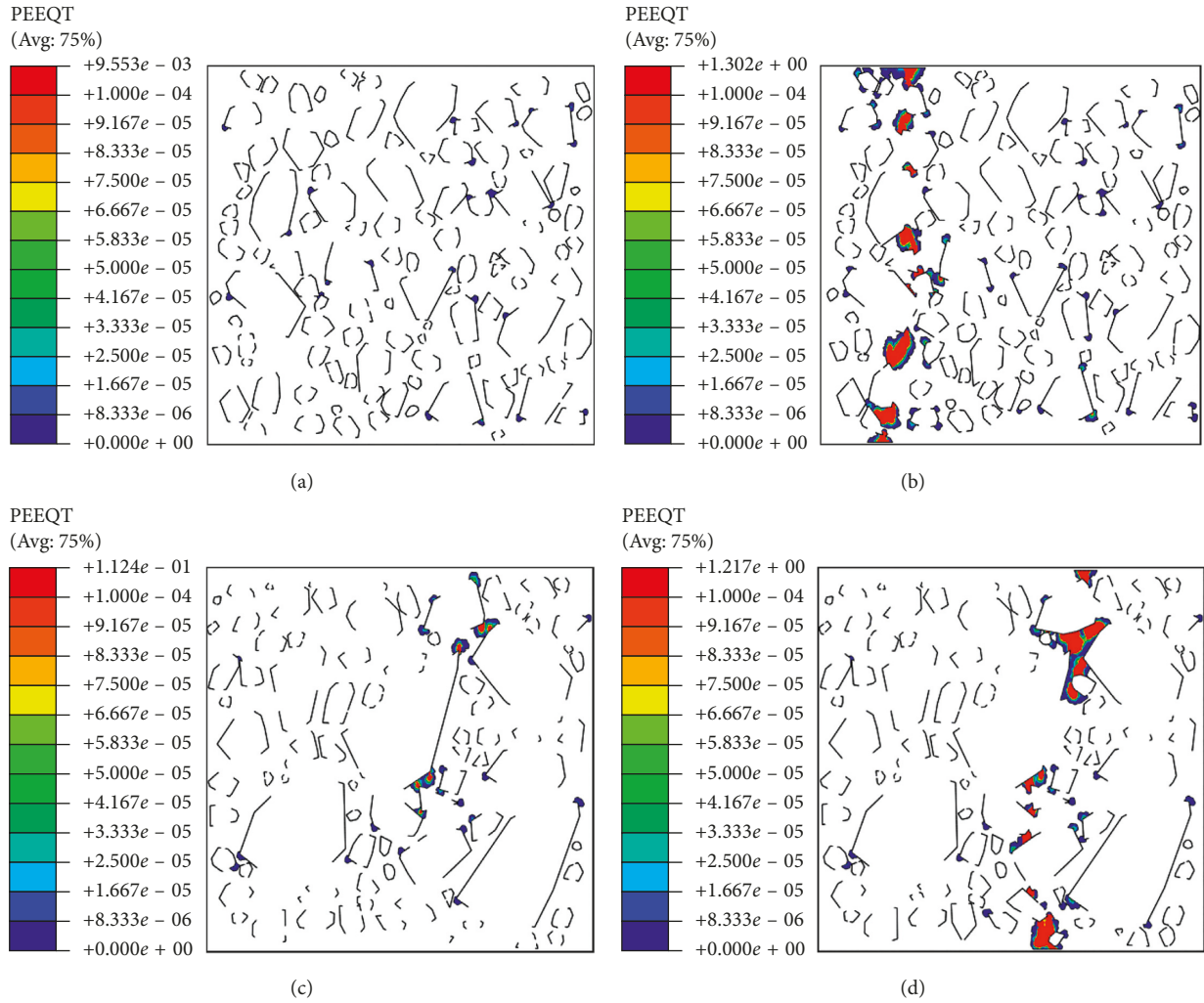


FIGURE 16: Distribution of tensile plastic strain on the mesoscale. At peak stress: (a) Type II; (c) Type III. At the maximum displacement: (b) Type II; (d) Type III.

Within the context of MCS, the sample number (the number of concrete specimens), which controls the accuracy of statistical characteristics and therefore should be large enough in order to meet the requirement of statistical convergence, can be taken as the smallest one needed to stabilize the values of statistical parameters with respect to the number of concrete specimens. On the contrary, for each specimen in the MCS, the corresponding macroscopic mechanical parameters related to concrete tensile fracturing behaviors, including tensile elastic modulus, peak stress (tensile strength), peak strain, and fracture energy, can be determined with ease based on the uniaxial tensile stress-strain (or displacement) curve obtained from the mesoscale FE modeling, and then, statistical analysis can be performed for each parameter mentioned above, providing the statistical characteristics of these parameters, including mean value (MV), standard deviation (SD), and coefficient of variation (CoV), which can be used as the basis of the subsequent comparative study.

4. Results and Discussion

The uniaxial tensile fracturing behaviors of hydraulic three-graded concrete with $A_F = 50\%$ in the sense of 2D and the

proportions of small, medium, and large coarse aggregate set to 0.3, 0.3, and 0.4, respectively, and the corresponding wet-screened concrete are compared in detail in this section.

4.1. Numerical Specimens and Mechanical Properties. As stated earlier, the differences in macroscopic mechanical parameters related to tensile fracturing behaviors of HFGC and the wet-screened concrete specimens are mainly attributed to three factors: specimen size variation, variation of gradation and volume fraction of coarse aggregate, and the weaker ITZs surrounding large coarse aggregates. In order to study the effects of these three factors, six types of numerical concrete specimens are generated in this study. For each type of numerical specimens, MCS is performed, and the specimen number is taken as 50 to satisfy the requirement of statistical convergence.

Numerical specimens in Type I with standard dimensions of $150\text{ mm} \times 150\text{ mm}$ are used to represent the wet-screened concrete specimens, while numerical specimens in Type II with dimensions of $300\text{ mm} \times 300\text{ mm}$ are generated to represent the wet-screened concrete specimens with the same size as the hydraulic three-graded concrete

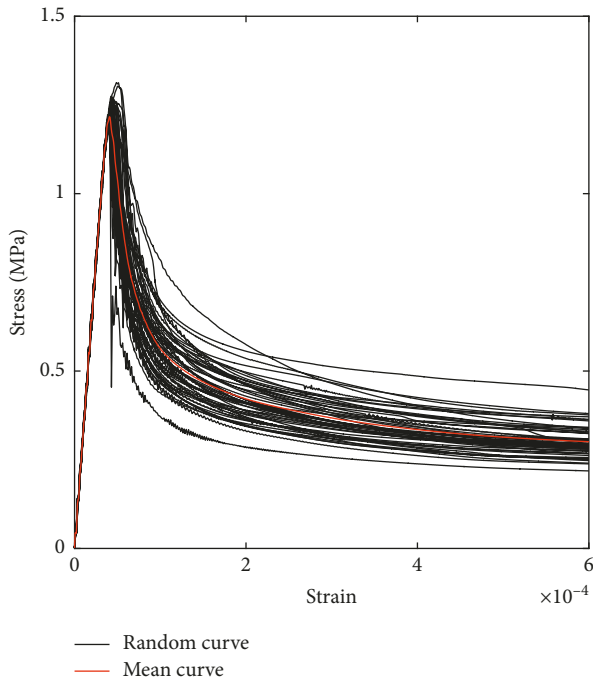


FIGURE 17: Macroscopic stress-strain curves and their mean curve of Type IV.

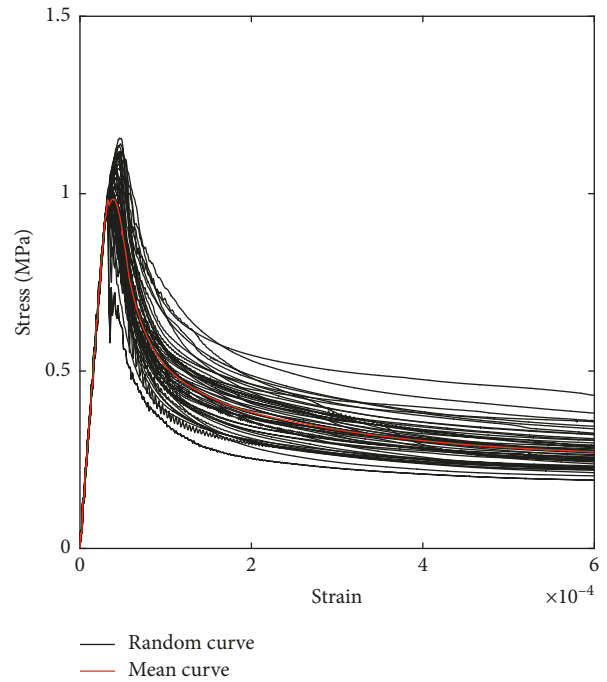


FIGURE 19: Macroscopic stress-strain curves and their mean curve of Type VI.

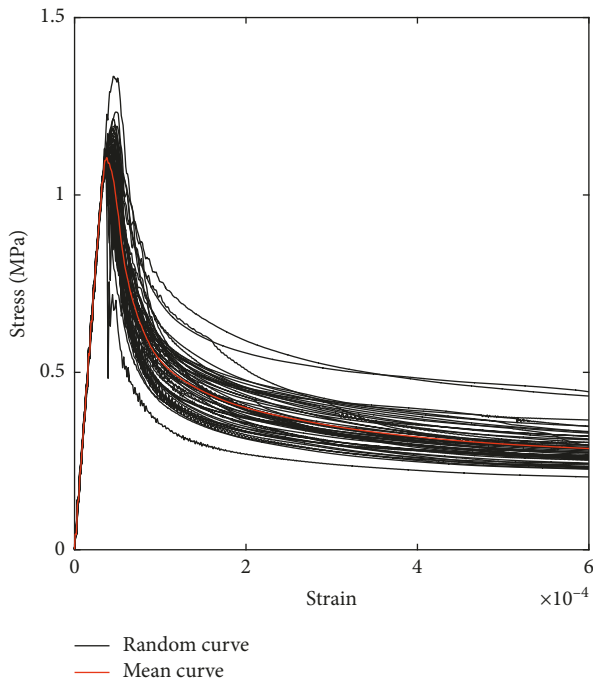


FIGURE 18: Macroscopic stress-strain curves and their mean curve of Type V.

specimens. Thus, by comparing the MCS results of Types I and II, the effect of specimen size variation can be extracted. Furthermore, by conducting the MCS of Type III consisting of the hydraulic three-graded concrete specimens with dimensions of 300 mm × 300 mm and with all ITZs assumed to having the same mechanical parameters and comparing the

MCS results of Types I and II, the effect of variation of gradation and volume fraction of coarse aggregate can be individually discussed. The numerical specimens in Types IV, V, and VI employ the same mesostructures as those of the numerical specimens in Type III, and the only difference lies in the mechanical properties of the ITZs surrounding large coarse aggregates (to be removed in the wet-screening process). For Type IV, the ratio of the mechanical properties of ITZs surrounding coarse aggregates with size larger than 40 mm to those of ITZs surrounding coarse aggregates with size no more than 40 mm is set to 90%, while for Types V and VI, the ratios are set to 80% and 70%, respectively. Thus, the effect of the long weaker ITZs can be roughly evaluated by comparing the MCS results of Types III, IV, V, and VI. Finally, by comparing the MCS results of Types I, II, III, IV, V, and VI, the combined effect of three factors on the differences of the investigated macroscopic mechanical parameters can be analyzed, and the governing factor(s) corresponding to each of these parameters can also be identified.

For each numerical specimen, uniaxial tensile fracturing simulation is performed. In all FE simulations, the left end of the specimen is fixed in the horizontal direction, while the opposite end is subjected to a uniformly distributed horizontal displacement up to 0.18 mm corresponding to 1200 microstrains for Type I or 600 microstrains for Types II, III, IV, V, and VI, namely, a displacement-controlled loading scheme is used. Following the strategy discussed in Section 3.3, the loading time is set to 0.036 s, which corresponds to a loading rate 5 mm/s.

According to the setup of numerical specimen type, only the mechanical properties of coarse aggregate, mortar, and

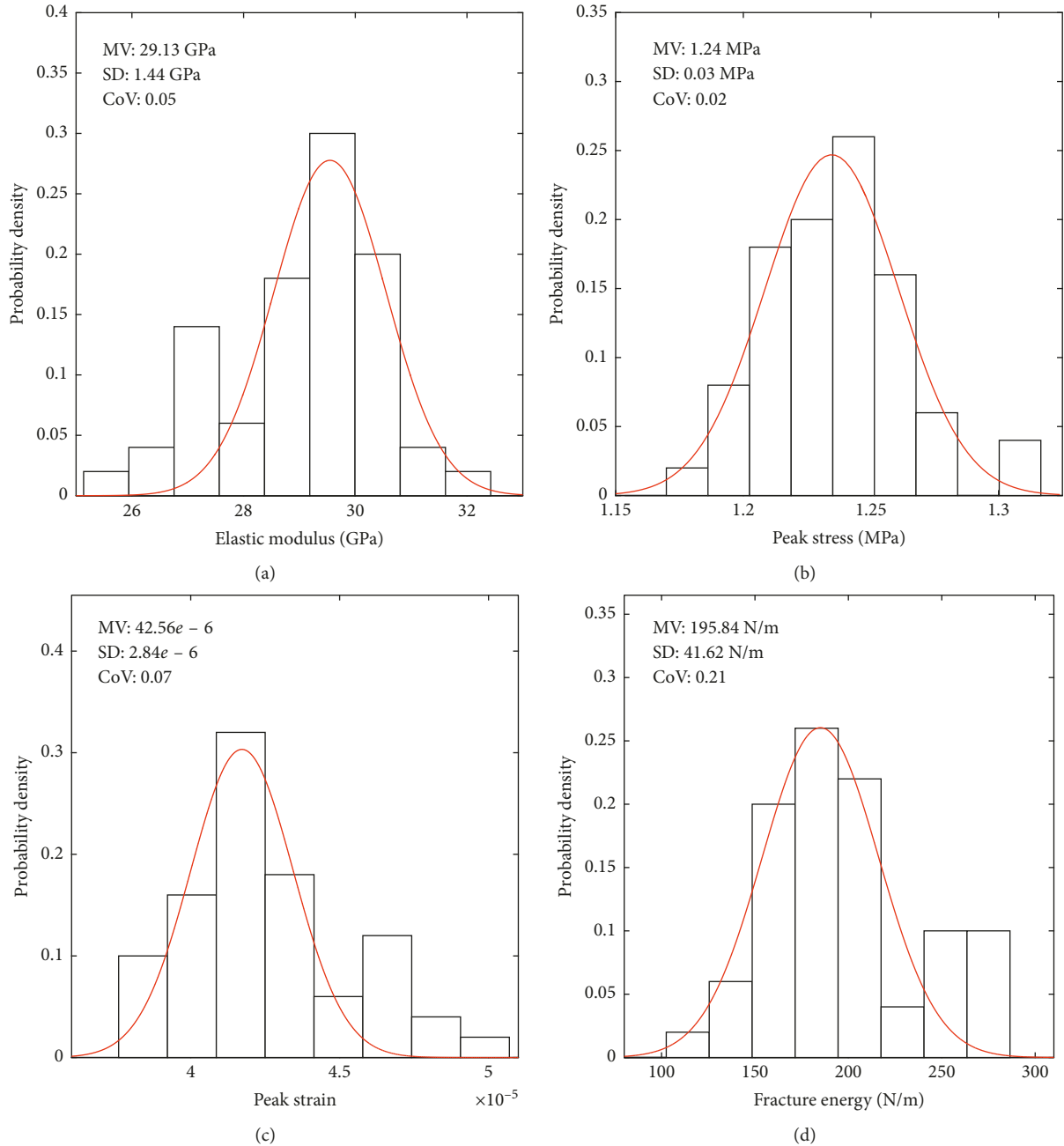


FIGURE 20: Probability density of macroscopic mechanical parameters related to tensile fracturing behaviors of Type IV. (a) Tensile elastic modulus. (b) Peak stress. (c) Peak strain. (d) Fracture energy.

ITZ in the wet-screened concrete are independent and should be defined in the mesoscale FE simulations. However, due to the lack of experimental results for ITZ, the compressive and tensile strengths and elastic modulus of ITZ are assumed to be 75% of those of mortar since ITZ is considered to be weaker than mortar, while the other mechanical properties of ITZ are taken as the same as those of mortar. Table 1 lists the mechanical properties of coarse aggregate, mortar, and ITZ adopted in this study. It is noted that the mechanical properties of mortar is directly obtained from the Chinese code GB 50010-2002 (the code for designing concrete structures), and the compression hardening

curve and the tension softening curve are shown in Figures 5 and 6, respectively.

4.2. Effect of Specimen Size Variation. The macroscopic stress-strain curves of all 50 specimens of Type I with the mean curve are plotted in Figure 7, and Figure 8 depicts the corresponding results of Type II. Overall, it can be observed that all the concrete specimens approximately exhibit linear elastic responses on the macroscale in the prepeak stage, whereas in the postpeak phase, the macroscopic stress decreases in a nonlinear way (softening) with the increase of

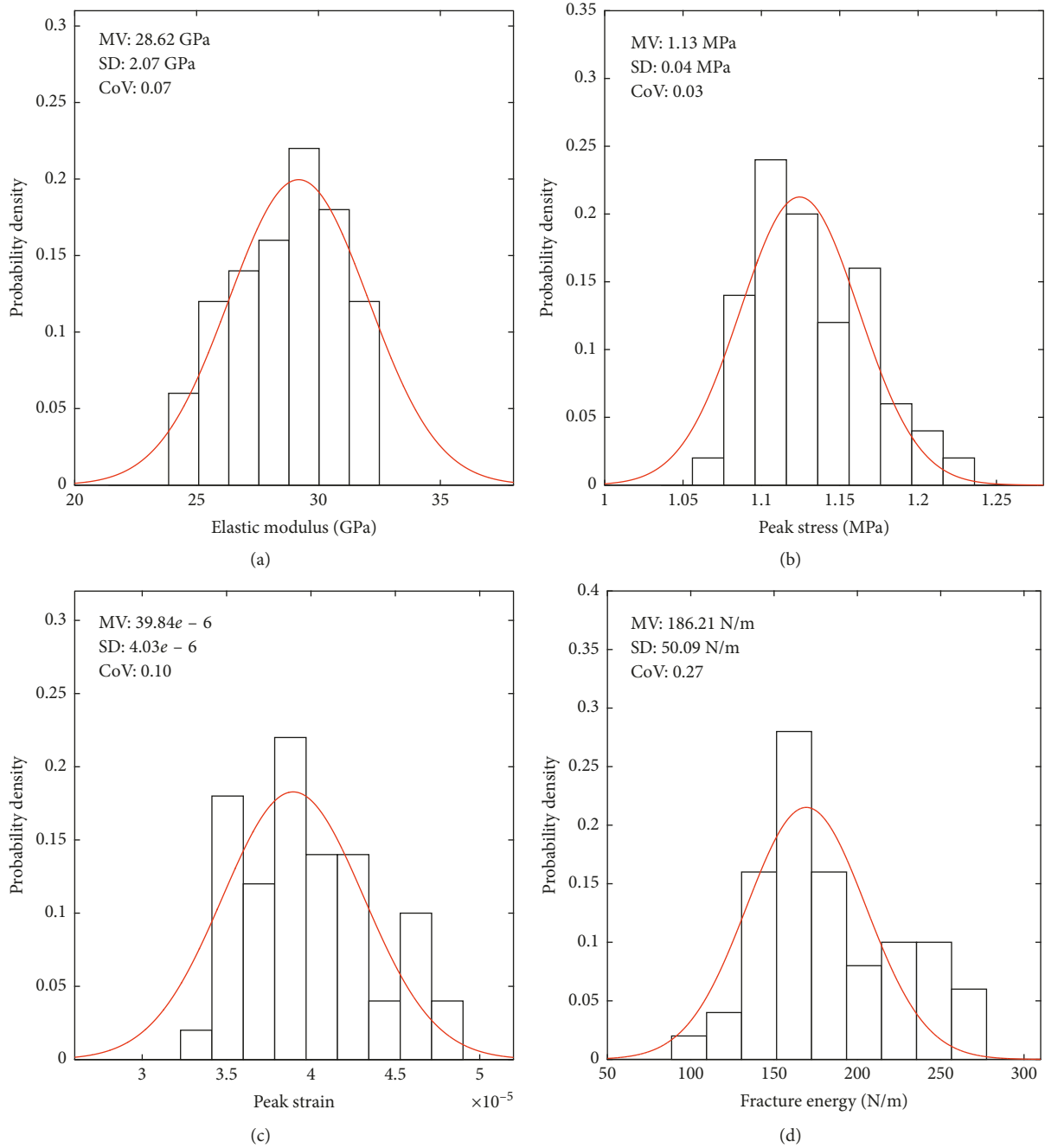


FIGURE 21: Probability density of macroscopic mechanical parameters related to tensile fracturing behaviors of Type V. (a) Tensile elastic modulus. (b) Peak stress. (c) Peak strain. (d) Fracture energy.

applied displacement, which can be attributed to the mesoscopic cracking taking place in ITZs and mortar. Furthermore, it is worth noting that although the elastic responses of all the specimens of Type I or Type II are quite close to each other, dispersion clearly appears during tensile softening, indicating the necessity of MCS.

With the peak stress, peak strain and fracture energy extracted from each stress-strain (displacement) curve, the statistical analysis of the investigated macroscopic parameters can be executed. Figure 9 presents the probability densities and the best fit Gaussian probability density

functions (PDFs) of the tensile elastic modulus, peak stress, peak strain, and fracture energy of Type I, together with MVs, SDs, and CoVs, whereas the statistical results of Type II are depicted in Figure 10. It is shown that the randomness of the investigated parameters can be roughly characterized by the Gaussian distribution. However, fracture energy is distinguished from elastic modulus, peak stress, and peak strain by its large CoV, which suggests that the random mesostructure has a bigger effect on fracture energy. With respect to each investigated macroscopic parameter, similar probability distributions can be found in Types I and II,

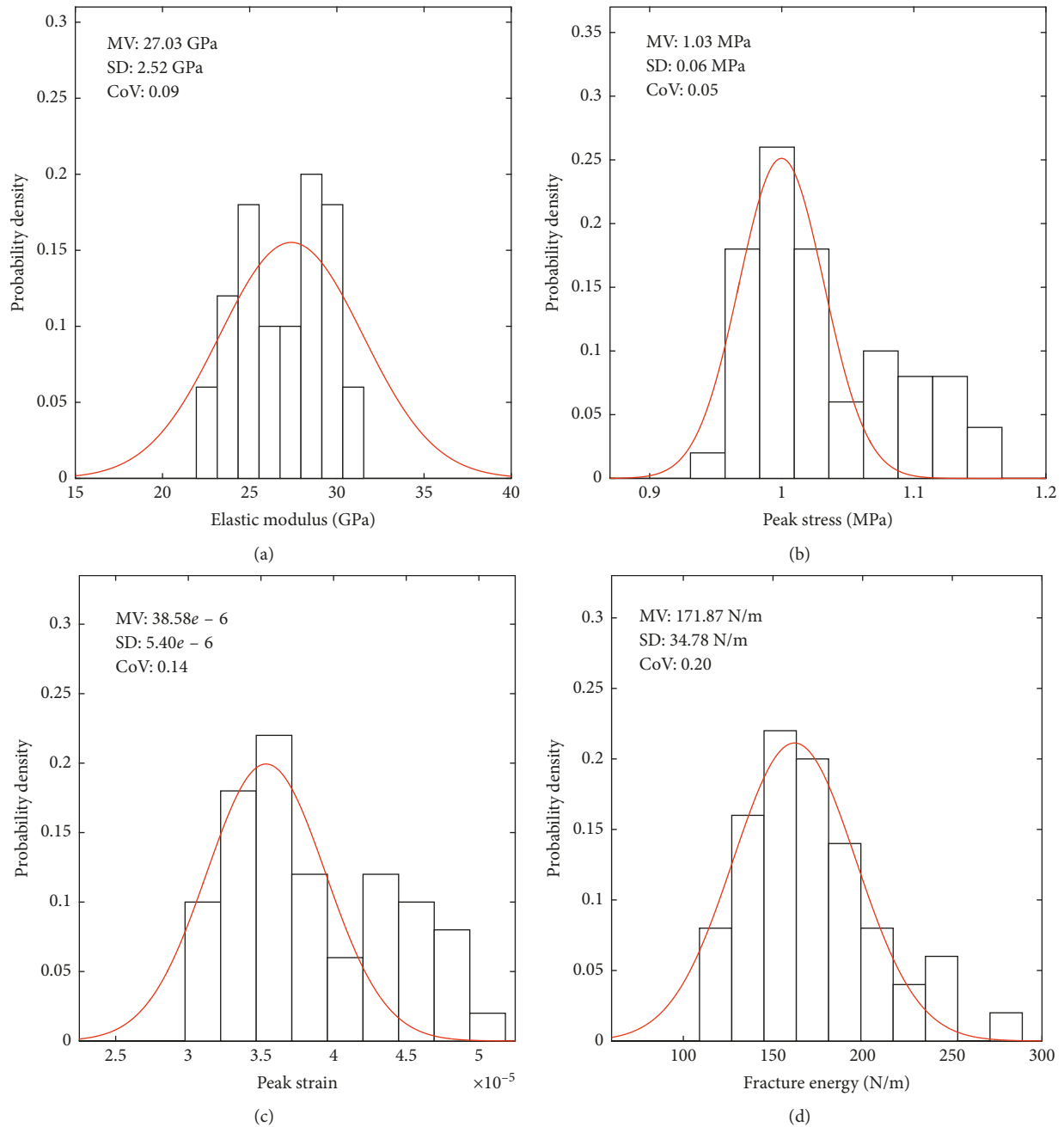


FIGURE 22: Probability density of macroscopic mechanical parameters related to tensile fracturing behaviors of Type VI. (a) Tensile elastic modulus. (b) Peak stress. (c) Peak strain. (d) Fracture energy.

which indicates the influence of the specimen size on the probability distributions of these parameters is not evident. Moreover, with the increase of the specimen size, different variations of the MVs of the investigated parameters can be observed. For the tensile elastic modulus and fracture energy, their MVs slightly increase with increasing specimen size (3.95% and 3.21%, respectively), whereas small MV reductions are shown for peak stress and peak strain (1.76% and 5.48%, respectively). On the whole, it can be concluded that the increase of the specimen size does result in the variations of the macroscopic mechanical parameters related to tensile fracturing behaviors, which is consistent with the

existing research results concerning the size effect of concrete [38]. However, in view of the large variation amplitudes of the investigated parameters obtained by limited experimental studies [11] (e.g., the typical ratio of the tensile strength of HFGC specimen to that of the corresponding wet-screened concrete specimen is ranging from 0.65 to 0.85), the variation of the specimen size is not a governing factor.

Figures 11 and 12 illustrate the variations of CoVs of tensile elastic modulus, peak stress, peak strain, and fracture energy with the sample number for Types I and II, respectively, from which it is noted that 50 random specimens are enough to achieve statistical convergence.

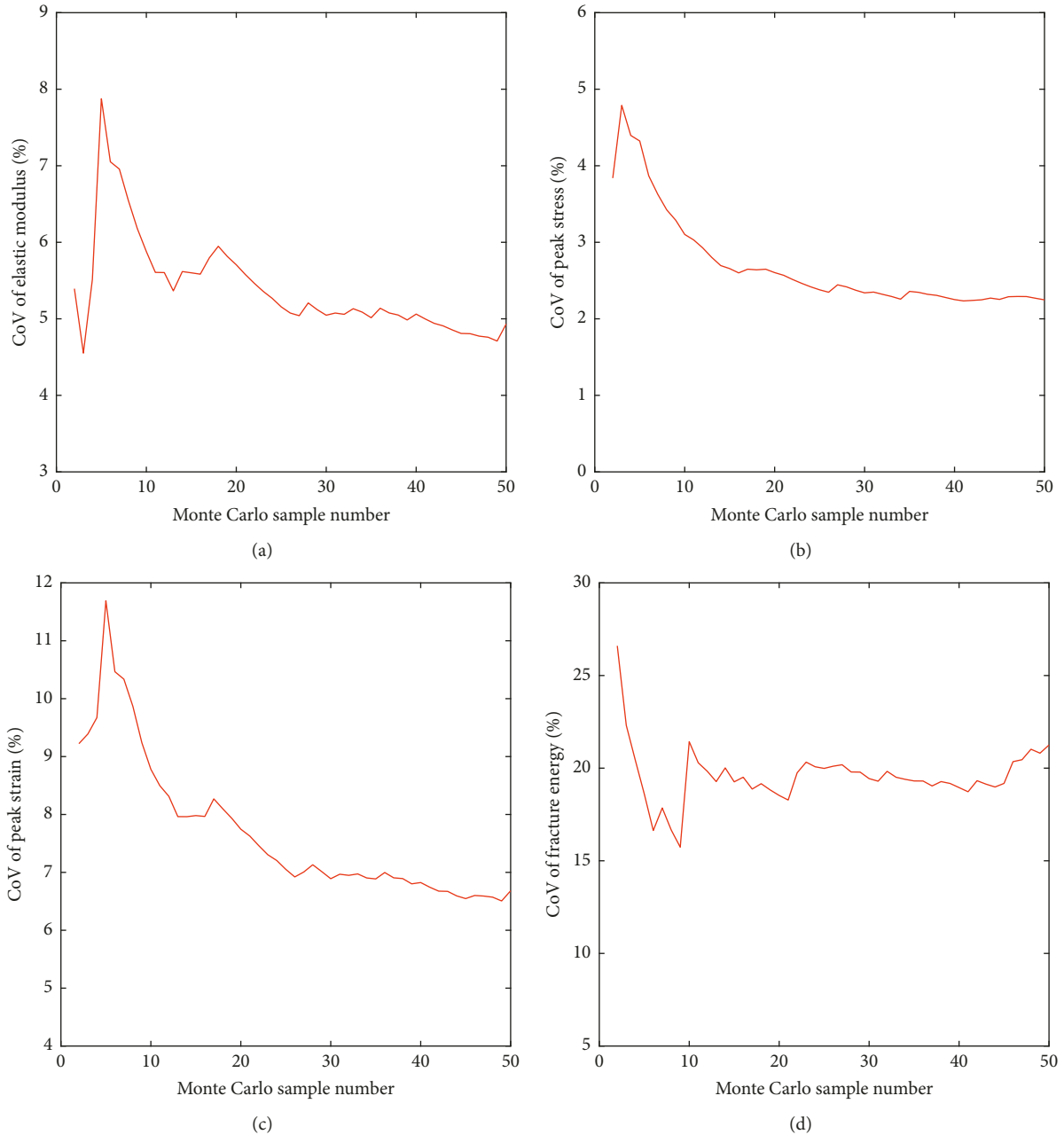


FIGURE 23: Influence of the sample number on CoV of macroscopic mechanical parameters of Type IV. (a) Tensile elastic modulus. (b) Peak stress. (c) Peak strain. (d) Fracture energy.

4.3. *Effect of Variation of Gradation and Volume Fraction of Coarse Aggregate.* The macroscopic stress-strain curves of all 50 specimens of Type III are drawn in Figure 13, along with the mean curve, and it is shown that the characteristic of the curves is similar to those of Type II.

Figure 14 demonstrates the probability densities and the best fit Gaussian probability density functions (PDFs) of the tensile elastic modulus, peak stress, peak strain, and fracture energy of Type III, with the calculated MVs, SDs, and CoVs. Also, it can be found that the randomness of the macroscopic parameters can be generally described by the Gaussian distribution, and the CoV of fracture energy is

much larger than that of tensile elastic modulus, peak stress, and peak strain. Compared to Type II, all calculated CoVs of Type III tend to decrease, which may be due to the increase of coarse aggregate volume fraction. For tensile elastic modulus, it is shown that its MV of Type III is clearly bigger than that of Type II (increased by 18.32%), which can be attributed to the existence of large coarse aggregates (much stiffer than mortar and ITZ) in HFGC. On the contrary, the MVs of peak stress, peak strain, and fracture energy of Type III are smaller than those of Type II (reduced by 3.65%, 18.73%, and 8.85%, respectively). Overall, the variation of gradation and volume fraction of coarse aggregate is found

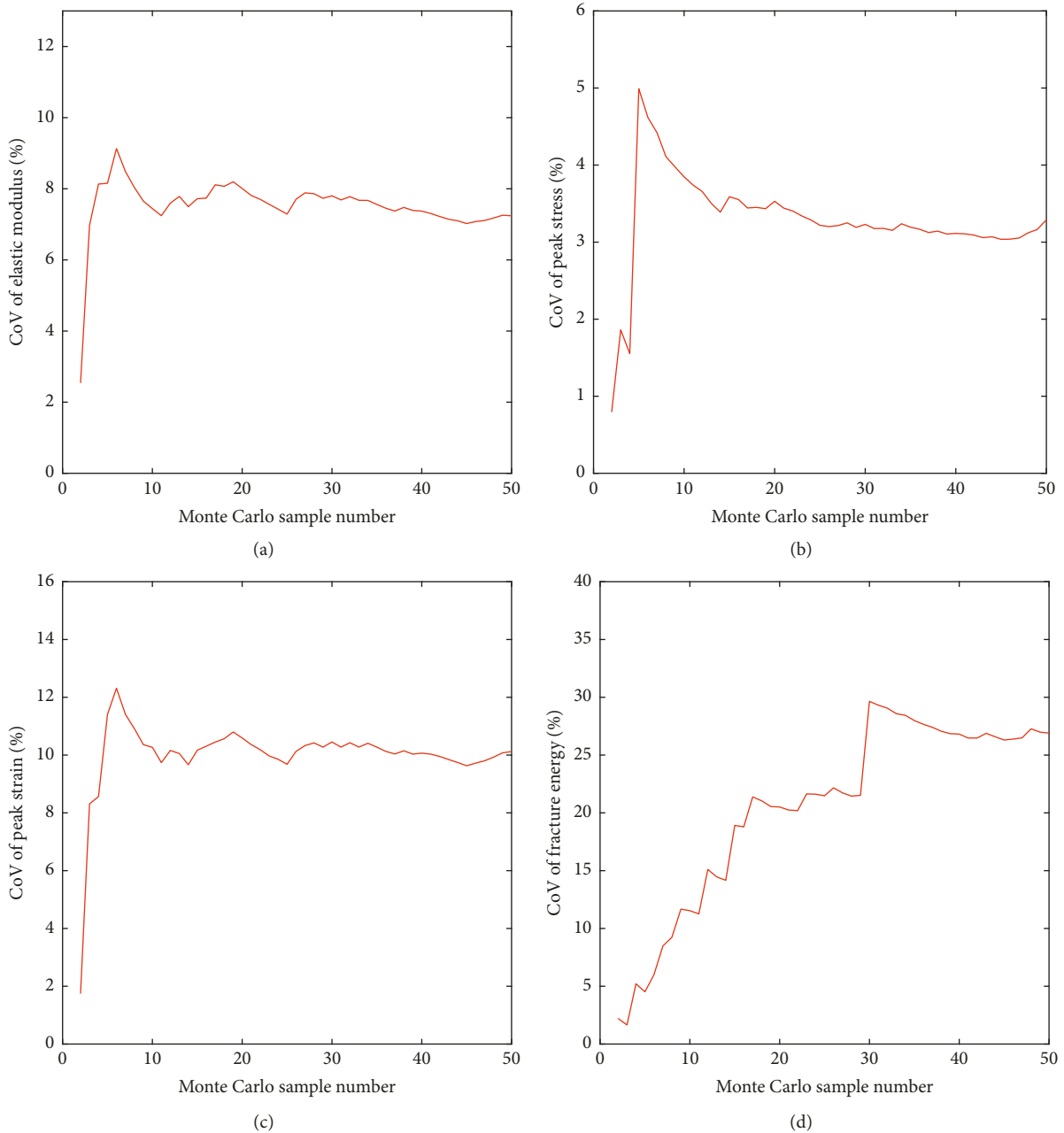


FIGURE 24: Influence of the sample number on CoV of macroscopic mechanical parameters of Type V. (a) Tensile elastic modulus. (b) Peak stress. (c) Peak strain. (d) Fracture Energy.

to give rise to big differences in the investigated parameters except peak stress and consequently can be considered to play an important role in the variations of tensile elastic modulus, peak strain, and fracture energy. Additionally, it is worth noting that specimen size variation and the variation of gradation and volume fraction of coarse aggregate have opposite effects on the variation of mean fracture energy.

The variations of CoVs of elastic modulus, peak stress, peak strain, and fracture energy with the number of samples for Type III are shown in Figure 15, from which it can also be concluded that the adopted sample number meets the requirement of statistical convergence.

To better understand the underlying differentiation mechanism on the mesoscale with respect to gradation and volume fraction, the elements with nonzero tensile plastic strain at peak stress and the maximum displacement of two typical specimens (one for Type II and the other for Type III) are visualized in Figure 16, in which the element with equivalent tensile plastic strain bigger than 100 microstrains is highlighted in red. It can be found that the majority of tensile cracks on the mesoscale is initiated in ITZs, and the subsequent propagation of mesoscale cracking is prone to take place and develop around the end of long ITZs (surrounding large coarse aggregates) due to their lower capacity

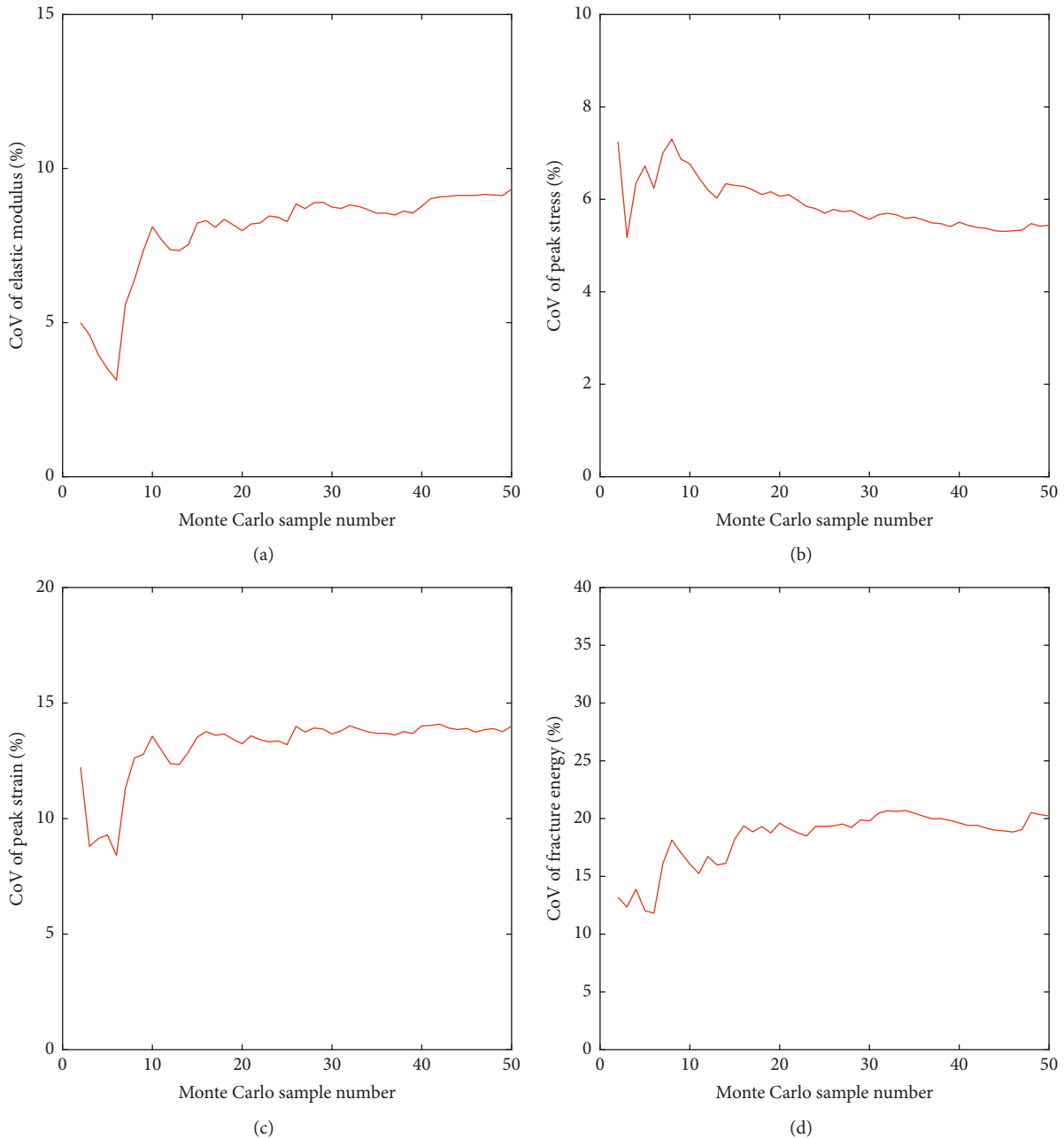


FIGURE 25: Influence of the sample number on CoV of macroscopic mechanical parameters of Type VI. (a) Tensile elastic modulus. (b) Peak stress. (c) Peak strain. (d) Fracture energy.

of resisting fracture compared to the short ITZs (around other coarse aggregates), leading to the lower peak stress of Type III. Moreover, it is shown that ITZs account for a bigger proportion of the macroscopic crack in the case of Type III compared to the Type II case, resulting in the lower fracture energy of Type III.

4.4. Effect of the Weaker ITZs Surrounding Large Coarse Aggregates. The macroscopic stress-strain curves with respect to Types IV, V, and VI, along with the corresponding mean curves, are illustrated in Figures 17–19, respectively. It

can be observed that the weakened mechanical properties of ITZs surrounding large coarse aggregates do not lead to significant change of characteristic of the macroscopic stress-strain relation, which can still be roughly divided into two stages: the prepeak linear stage and the postpeak softening stage.

The statistical results of the tensile elastic modulus, peak stress, peak strain, and fracture energy of Types IV, V, and VI are given in Figures 20–22, respectively. It is shown that the Gaussian distribution generally remains suitable for describing the randomness of these macroscopic parameters, and the dispersion of fracture energy is still much

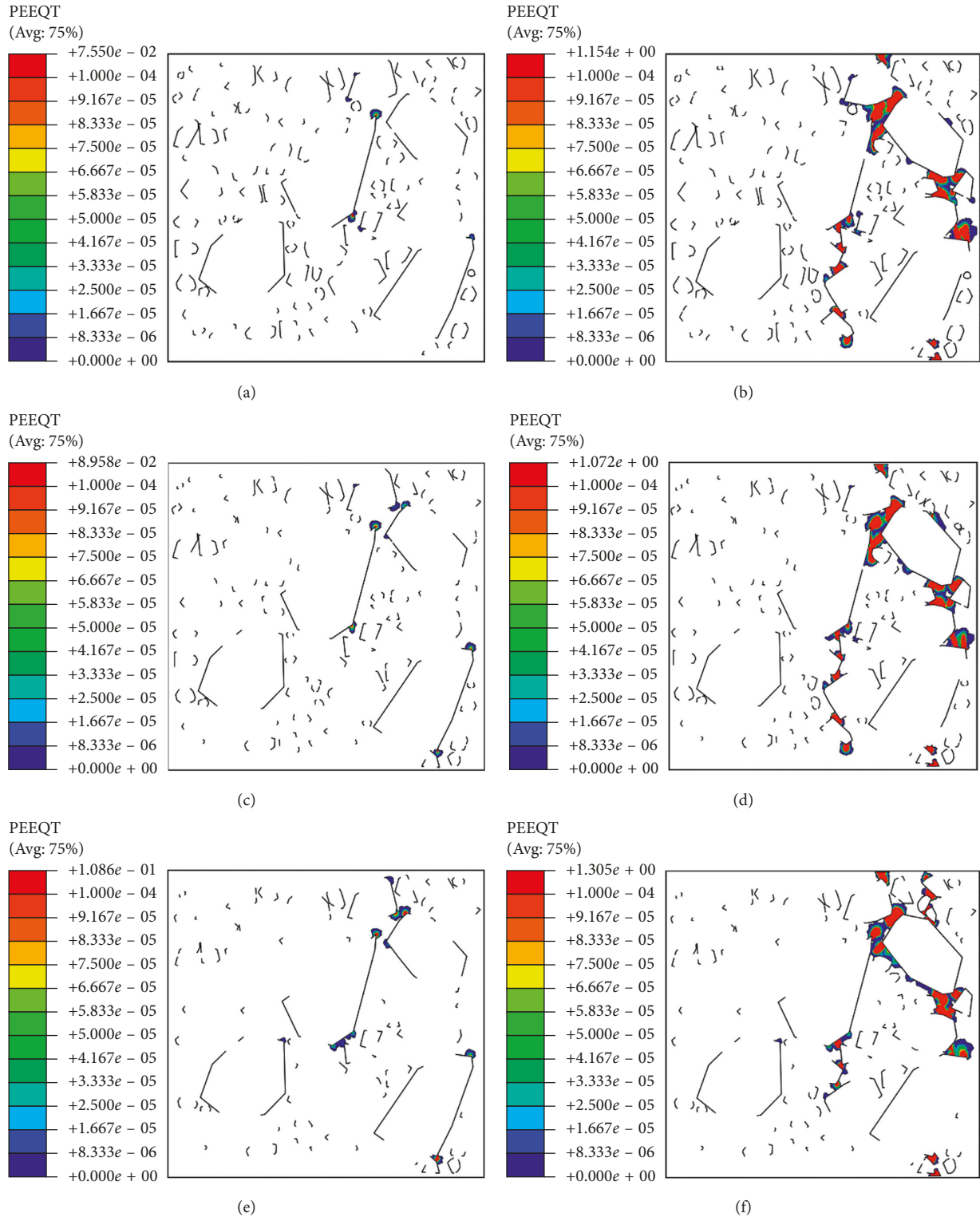


FIGURE 26: Distribution of tensile plastic strain on the mesoscale. At peak stress: (a) Type IV; (c) Type V; (e) Type VI. At the maximum displacement: (b) Type IV; (d) Type V; (f) Type VI.

higher than that of the other three parameters. Moreover, the dispersion of the investigated parameters tends to increase as the mechanical properties of the long ITZs gradually weakened, whereas tensile elastic modulus, peak

stress, peak strain, and fracture energy all suffer decreased MV. Compared to Type III, the MVs of tensile elastic modulus, peak stress, peak strain, and fracture energy of Type VI are decreased by 6.76%, 23.53%, 17.03%, and

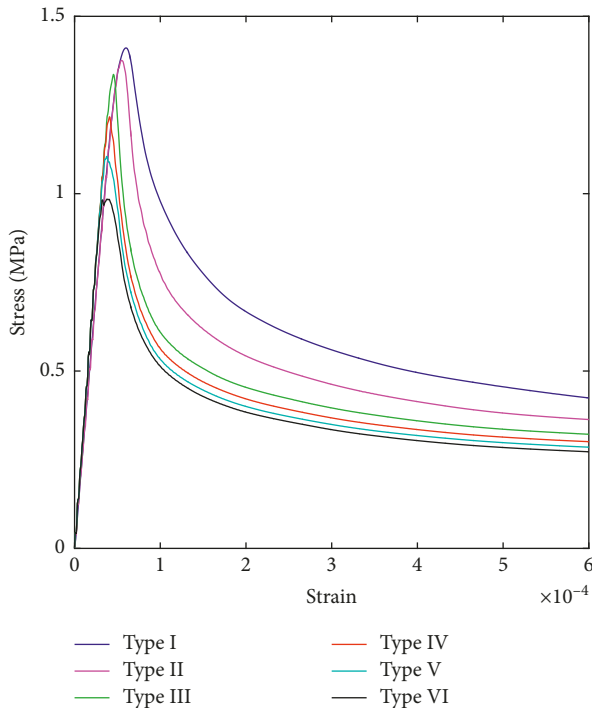


FIGURE 27: Macroscopic mean stress-strain curves of Types I, III, IV, V, and VI.

13.64%, respectively. On the whole, all the investigated parameters show significant change in response to the weaker ITZs surrounding large coarse aggregates and consequently should be considered to play a key role in the differences in the investigated parameters.

Again, it can be observed from Figures 23–25 that the number of specimens (50) is sufficient to reach converged results for Types IV, V, and VI.

Furthermore, to reveal the differentiation mechanism induced by the weaker ITZs surrounding large coarse aggregates, the elements with nonzero tensile plastic strain at peak stress and the maximum displacement of three specimens with the same mesostructure as the one illustrated in Figures 16(c) and 16(d) but different mechanical properties of ITZs surrounding large coarse aggregates, which belong to Types IV, V, and VI, respectively, are sketched in Figure 26. Although the long weaker ITZs definitely give rise to the decrease of tensile elastic modulus, the resulting lower load bearing capacity still reaches to its peak value (represented by peak stress) at a smaller macroscopic strain (peak strain), which is responsible for fewer aggregate-mortar interfacial cracks on the mesoscale (Figures 16(c), 26(a), 26(c), and 26(e)). On the contrary, as the long ITZs become weaker, the number of mesoscale cracks at the maximum displacement gradually decreases (Figures 16(d), 26(b), 26(d), and 26(f)), which means the existence of long weaker ITZs will suppress to a certain degree the development of mesoscale cracking in other regions and consequently leads to less energy dissipation.

4.5. Discussion on the Combined Effect and the Governing Factor(s). The mean stress-strain curves of Types I, II, III,

IV, V, and VI are plotted in Figure 27, and the PDFs of these types with respect to tensile elastic modulus, peak stress, peak strain, and fracture energy, with MVs, SDs, and CoVs, are shown in Figure 28.

Even though the consideration of the long weaker ITZs in HFGC results in the decrease of its tensile elastic modulus, it is shown in Figure 27 that the mean tensile elastic modulus of HFGC is still bigger than that of the corresponding wet-screened concrete. Furthermore, since the increase of tensile elastic modulus caused by increased specimen size is relatively small, the variation of gradation and volume fraction of coarse aggregate should be viewed as the governing factor of the difference in the mean tensile elastic modulus. Unlike tensile elastic modulus, the mean peak stress of HFGC is much smaller than that of the corresponding wet-screened concrete, and all the three factors are responsible for this observation in the same direction. However, the effect of the weaker ITZs surrounding large coarse aggregates is much more significant than that of the other two factors and therefore plays a governing role. Similarly, the mean peak strain of HFGC is much smaller compared to that of the corresponding wet-screened concrete, and each of the three factors plays a positive role in this regard. As the effect of increased specimen size on the decrease of mean peak strain is small, the other two factors, especially the variation of aggregate gradation and coarse aggregate content, dominate the difference in the mean peak strain. In addition, although the increased specimen size leads to a small increase in the mean fracture energy (obtained from the stress-displacement curve rather than the stress-strain curve shown in Figure 27), it is found that the mean fracture energy of HFGC is lower than that of the corresponding wet-screened concrete. Since either the variation of aggregate gradation and coarse aggregate content or the long weaker ITZs decrease the mean fracture energy to a relatively large extent, these two factors are viewed to be dominant in this respect. On the whole, although the MVs of tensile elastic modulus, peak stress, peak strain, and fracture energy caused by the wet-screened method indeed show significant change in response to wet-screening, different governing factor(s) can be identified for different mechanical parameters.

Regarding the dispersion of the investigated parameters, it is shown in Figure 28 that the effects of these factors differ from each other. Specifically, the effect of specimen size variation is quite small, and the effects of the other two factors are relatively larger. The dispersions of the investigated parameters of HFGC are found to be lower than those of the corresponding wet-screened concrete when taking into consideration only the variation of gradation and volume fraction of coarse aggregate, while an opposite effect of the weaker ITZs surrounding large coarse aggregates on the dispersions can be observed. In view of the fact that the dispersion of each of the investigated parameters of HFGC is clearly higher than that of the corresponding wet-screened concrete due to the combined effect of three main factors, the weaker ITZs surrounding large coarse aggregates are considered to be the key factor controlling the dispersion variations of the investigated parameters.

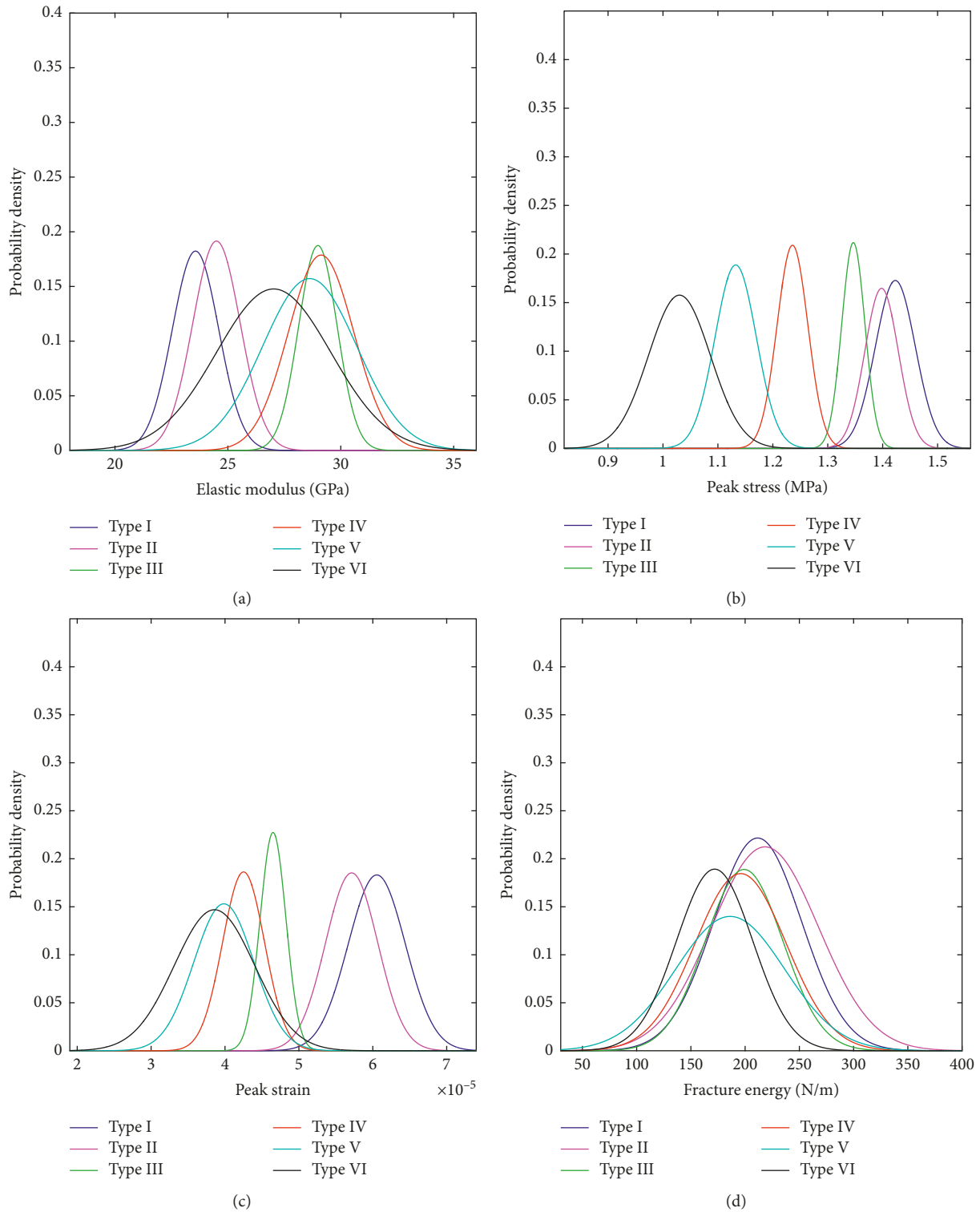


FIGURE 28: Probability densities of macroscopic mechanical parameters related to tensile fracturing behaviors of Types I, II, III, IV, V, and VI. (a) Tensile elastic modulus. (b) Peak stress. (c) Peak strain. (d) Fracture energy.

5. Conclusions

A finite element mesoscale modeling methodology for hydraulic fully graded and wet-screened concretes is first proposed in the present work. Then, based on the mesoscale

FE modeling and extensive Monte Carlo simulations, a detailed comparative study on the tensile fracturing behaviors of fully graded and wet-screened concretes is carried out with prime attention placed on the individual and combined effects of three main factors, namely, specimen size variation,

variation of gradation and volume fraction of coarse aggregate, and the weaker ITZs surrounding large coarse aggregates. The work results in the following conclusions:

- (i) It is shown that the tensile fracturing behaviors of hydraulic fully graded and wet-screened concretes are clearly sensitive to the internal material structure, which necessitates the extensive Monte Carlo simulations performed in this study.
- (ii) All the investigated macroscopic mechanical parameters related to tensile fracturing behaviors, that is, tensile elastic modulus, peak stress, peak strain, and fracture energy, show significant change in response to wet-screening, even though the characteristics of the stress-strain (or displacement) relation of hydraulic fully graded concrete are similar to those of the wet-screened concrete.
- (iii) The mean tensile elastic modulus of hydraulic fully graded concrete is found to be larger than that of the corresponding wet-screened concrete, which is mainly due to the variation of gradation and volume fraction of coarse aggregate.
- (iv) Owing to the existence of the long weaker ITZs in hydraulic fully graded concrete, the mean peak stress of hydraulic fully graded concrete is smaller than that of the corresponding wet-screened concrete.
- (v) Both the variation of gradation and volume fraction of coarse aggregate and the long weaker ITZs are considered to lead to a smaller mean peak strain of hydraulic fully graded concrete compared to the corresponding wet-screened concrete.
- (vi) It is found that the mean fracture energy of hydraulic fully graded concrete is lower than that of the corresponding wet-screened concrete and the variation of gradation and volume fraction of coarse aggregate and the long weaker ITZs are identified to be the governing factors.
- (vii) The degree of dispersion of the investigated parameters of HFGC is found to be higher than that of the corresponding wet-screened concrete, and the long weaker ITZs can be considered to play a dominant role in this respect.

Data Availability

The datasets generated during and/or analyzed during the current study are available from the corresponding author on reasonable request.

Conflicts of Interest

The authors declare that there are no conflicts of interest regarding the publication of this paper.

Acknowledgments

This work was supported by projects of the National Natural Science Foundation of China (Grant nos. 51739006 and

U1765204) and by “the Fundamental Research Funds for the Central Universities” (Grant no. 2018B11414).

References

- [1] J. Lu, S. Huang, and L. Zp, “Statistical analysis of limit tensile strain of full graded concrete samples,” *Journal of Hohai University*, vol. 26, pp. 101–104, 1998.
- [2] Y. Dong, K. Xiao, and H. Yang, “Experimental studies on properties of fully-graded arch dam concrete with natural aggregate,” *Chinese Journal of Concrete*, vol. 2013, pp. 140–143, 2013.
- [3] D. Zheng, W. Han, and Y. Zhang, “Research on strength ratio of full grade and wet-sieving hydraulic concrete,” *Chinese Journal of Water Resources and Architectural Engineering*, vol. 9, pp. 10–14, 2011.
- [4] M. Paggi, G. Ferro, and F. Braga, “A multiscale approach for the seismic analysis of concrete gravity dams,” *Computers and Structures*, vol. 122, pp. 230–238, 2013.
- [5] L. Xu, S. Jing, J. Liu, and Y. Huang, “Cracking behavior of a concrete arch dam with weak upper abutment,” *Mathematical Problems in Engineering*, vol. 2017, Article ID 6541975, 13 pages, 2017.
- [6] Y. Xiao, “Study on the real compressive strength of high-arch dam concrete,” *Chinese Journal of Water Power*, vol. 36, pp. 103–105, 2010.
- [7] T. Tang, S. Duan, and D. Yi, “Analysis on full-graded and wet-screened tests for Jinping I Arch dam concrete,” *Chinese Journal of Yellow River*, vol. 34, pp. 111–112, 2012.
- [8] J. Xie, Y. Tang, and G. Chen, “Study on the properties of concrete for arch dam of Xiaowan Hydropower Station,” *Chinese Journal of Water Power*, vol. 35, pp. 38–41, 2009.
- [9] H. Yang, M. Rao, and Y. Dong, “Influence study of extra-large stone limited size and content on full-graded concrete properties,” *Construction and Building Materials*, vol. 127, pp. 774–783, 2016.
- [10] A. Sajna and H. Linsbauer, “Fracture mechanics of mass concrete–wet-screening procedure (FMWS),” *Fracture Mechanics of Concrete Structures*, vol. 1, pp. 101–110, 1998.
- [11] C. Serra, A. Batista, and N. M. Azevedo, “Dam and wet-screened concrete creep in compression: in situ experimental results and creep strains prediction using model B3 and composite models,” *Materials and Structures*, vol. 49, no. 11, pp. 4831–4851, 2016.
- [12] R. Blanks and C. McNamara, “Mass concrete tests in large cylinders,” *ACI Journal Proceedings*, vol. 31, pp. 280–303, 1935.
- [13] W. Liu, W. Ye, H. Ge, and N. Xie, “Experimental study on mechanical properties of full graded concrete of Dongjiang dam,” *Chinese Journal of Water Resources and Hydropower Engineering*, vol. 1986, pp. 8–14, 1986.
- [14] G. Huang, “Experimental research of full-graded mass concrete strength,” *Chinese Journal of Water Power*, vol. 1992, pp. 45–48, 1992.
- [15] Z. Yang and R. Chen, “Experimental study on mechanical properties of fully graded aggregate concrete in TGP,” *Chinese Journal of Yangtze River Scientific Research Institute*, vol. 15, pp. 1–5, 1998.
- [16] G. Li, Z. Yang, and D. Yang, “Experimental research on mechanical properties of full graded mass concrete for high arch dams,” *Chinese Journal of China Three Gorges University*, vol. 25, pp. 500–503, 2003.
- [17] Z. Deng, Q. Li, and H. Fu, “Tensile and compressive behaviors of full grade concrete made of crushed coarse aggregate,” *Chinese Journal of Hydraulic Engineering*, vol. 36, pp. 214–218, 2005.

- [18] Z. Deng, Q. Li, and H. Fu, "Comparison between mechanical properties of dam and sieved concretes," *Chinese Journal of Materials in Civil Engineering*, vol. 20, no. 4, pp. 321–326, 2008.
- [19] C. Serra, A. L. Batista, and N. Monteiro Azevedo, "Effect of wet screening in the elastic properties of dam concrete: experimental in situ test results and fit to composite models," *Journal of Materials in Civil Engineering*, vol. 28, no. 12, p. 04016146, 2016.
- [20] L. Shi, L. Wang, Y. Song, and L. Shen, "Dynamic properties of large aggregate concrete under triaxial loading," *Magazine of Concrete Research*, vol. 67, no. 6, pp. 282–293, 2015.
- [21] C. Serra, A. L. Batista, N. M. Azevedo, and J. Custódio, "Prediction of dam concrete compressive and splitting tensile strength based on wet-screened concrete test results," *Journal of Materials in Civil Engineering*, vol. 29, no. 10, p. 04017188, 2017.
- [22] G. Cusatis, D. Pelessone, and A. Mencarelli, "Lattice discrete particle model (LDPM) for failure behavior of concrete. I: theory," *Cement and Concrete Composites*, vol. 33, no. 9, pp. 881–890, 2011.
- [23] G. Cusatis, A. Mencarelli, D. Pelessone, and J. Baylot, "Lattice discrete particle model (LDPM) for failure behavior of concrete. II: calibration and validation," *Cement and Concrete Composites*, vol. 33, no. 9, pp. 891–905, 2011.
- [24] X. Wang, M. Zhang, and A. P. Jivkov, "Computational technology for analysis of 3D meso-structure effects on damage and failure of concrete," *International Journal of Solids and Structures*, vol. 80, pp. 310–333, 2016.
- [25] P. Wriggers and S. Moftah, "Mesoscale models for concrete: homogenisation and damage behaviour," *Finite Elements in Analysis and Design*, vol. 42, no. 7, pp. 623–636, 2006.
- [26] X. Du, L. Jin, and G. Ma, "Numerical simulation of dynamic tensile-failure of concrete at meso-scale," *International Journal of Impact Engineering*, vol. 66, pp. 5–17, 2014.
- [27] Y. Huang, Z. Yang, W. Ren, G. Liu, and C. Zhang, "3D meso-scale fracture modelling and validation of concrete based on in-situ X-ray computed tomography images using damage plasticity model," *International Journal of Solids and Structures*, vol. 67–68, pp. 340–352, 2015.
- [28] X. Wang, Z. Yang, J. Yates, A. Jivkov, and C. Zhang, "Monte Carlo simulations of mesoscale fracture modelling of concrete with random aggregates and pores," *Construction and Building Materials*, vol. 75, pp. 35–45, 2015.
- [29] R. Rezaekhiani and G. Cusatis, "Asymptotic expansion homogenization of discrete fine-scale models with rotational degrees of freedom for the simulation of quasi-brittle materials," *Journal of the Mechanics and Physics of Solids*, vol. 88, pp. 320–345, 2016.
- [30] K. Kim and Y. Lim, "Simulation of rate dependent fracture in concrete using an irregular lattice model," *Cement and Concrete Composites*, vol. 33, no. 9, pp. 949–955, 2011.
- [31] Z. Bažant, M. Tabbara, M. Kazemi, and G. Pijaudier-Cabot, "Random particle model for fracture of aggregate or fiber composites," *Journal of Engineering Mechanics*, vol. 116, no. 8, pp. 1686–1705, 1990.
- [32] J. Walraven and H. Reinhardt, "Theory and experiments on the mechanical behaviour of cracks in plain and reinforced concrete subjected to shear loading," *Heron*, vol. 26, no. 1, 1981.
- [33] Z. Wang, A. Kwan, and H. Chan, "Mesoscopic study of concrete I: generation of random aggregate structure and finite element mesh," *Computers and Structures*, vol. 70, no. 5, pp. 533–544, 1999.
- [34] L. Xu and Y. Huang, "Effects of voids on concrete tensile fracturing: a mesoscale study," *Advances in Materials Science and Engineering*, vol. 2017, pp. 1–14, 2017.
- [35] J. Unger and S. Eckardt, "Multiscale modeling of concrete," *Archives of Computational Methods in Engineering*, vol. 18, no. 3, pp. 341–393, 2011.
- [36] ABAQUS, *ABAQUS 6.5 User's Manual*, ABAQUS Inc., Johnston, RI, USA, 2004.
- [37] J. Lee and G. L. Fenves, "Plastic-damage model for cyclic loading of concrete structures," *Journal of Engineering Mechanics*, vol. 124, no. 8, pp. 892–900, 1998.
- [38] Z. P. Bažant, "Size effect in blunt fracture: concrete, rock, metal," *Journal of Engineering Mechanics*, vol. 110, no. 4, pp. 518–535, 1984.

